

UNIVERSITEIT ANTWERPEN

Faculteit Wetenschappen

Departement Fysica

Multivortex states in mesoscopic superconducting squares and triangles

Proefschrift voorgelegd tot het behalen van de graad van
licentiaat Natuurkunde
aan de Universiteit Antwerpen te verdedigen door

Haijun Zhao

Promotor: Prof. dr. F. M. Peeters

Co-promotor: Dr. V. R. Misko

Antwerpen, 2007

Acknowledgements

I would like to express my gratitude to all those who gave me the opportunity to complete this thesis. I gratefully acknowledge my promotor, Prof. Dr. François M. Peeters for offering me the opportunity to do my advanced master thesis in his group and leading me to the new fascination world. His truly scientist intuition has made him as a constant oasis of ideas and passions in science, which exceptionally inspire me and enrich my growth as a student, a researcher and a scientist I want to be.

Also I would like to thank Slave for his help, stimulating suggestions and encouragement during the whole thesis progress. It is also a good opportunity to thank my office-mates Golib, Vladan, Ben, Sergio and Hao, who offered me a positive working atmosphere and lots of good advice.

I am indebted to all my teachers. Particular thanks to Prof. dr. J. Tempere and Prof. dr. F. Brosens, for their wise advice on my research work.

I wish to thank Zhengzhong Zhang, Yajiang Chen, Li Bin and Michael who offered me a lot of help. Special thanks go to Roeland for science discussion. Also thanks to my classmates Xiangyong Zhou, Haiyan Tan, Binjie Wang, Kamal and Nissy who enjoy this long process with me and give me sincere friendship and great support.

Lastly, and most importantly, I wish to thank my parents, who brought me up, and teach me, help me and always do their best to support me.

Contents

1	Introduction: Nucleation of superconductivity and vortex states in mesoscopic superconductors	3
1.1	Mesoscopic superconductors: a competition between the vortex-vortex interaction and the effect of boundaries	4
1.2	Vortex states in mesoscopic disks	4
1.3	Symmetry-induced vortex states in mesoscopic superconductors with noncircular geometries	7
1.4	Superconductivity in mesoscopic squares and triangles	9
2	Vortex states in rectangles	13
2.1	Theoretical approach	13
2.1.1	The London equation	13
2.1.2	Image technique applied for solving the London equation	16
2.1.3	Solution of the London equation for a rectangle	20
2.2	Numerical results	28
2.2.1	The free energy distribution	28
2.2.2	Vortex patterns in square samples	30
2.2.3	Comparison with experiment	39
3	Vortex states in equilateral triangles	40
3.1	Theoretical formalism	40
3.1.1	Solution of the London equation for an equilateral triangle	40
3.2	Numerical results	43
3.2.1	Meissner state in triangular samples	43
3.2.2	Vortex patterns in triangular samples	43
3.2.3	Comparison with experiment	47
4	Conclusions	48

Chapter 1

Introduction: Nucleation of superconductivity and vortex states in mesoscopic superconductors

With decreasing dimensions, the effect of the surface on the nucleation of the superconductivity, on the formation and penetration of vortices into a sample, and on the interactions (vortex-vortex and surface-vortex) becomes increasingly important. The sample geometry plays a crucial role leading to an enhancement of superconductivity, i.e., the superconducting critical parameters: the critical magnetic field, H_c , the critical current, J_c , and the critical temperature, T_c (note that the latter is realized only in very small (nanometer-scale) samples where the energy levels of the electron motion are quantized).

In mesoscopic superconductors with sizes comparable to the characteristic lengths, i.e., the coherence length ξ and the magnetic field penetration depth λ , the critical field H_c is enhanced and can exceed the (surface) critical field H_{c3} [1, 2], as shown experimentally and theoretically for Al square loops [3, 4], disks [5–9], triangles [10–13], and Pb 3D multi-cone-shaped nano-bridges [14, 15]. The observed phenomena have been theoretically treated within the Ginzburg-Landau (GL) and London theories. The interesting effects are induced by samples' boundaries, e.g., the boundary condition on the superconduction wave function. These surfaces are also important for the penetration and expulsion of the vortices. The interplay between the C_∞ -symmetry of the magnetic field and the discrete symmetry of the sample can lead to a symmetrically-confined vortex matter accompanied by spontaneous generation of antivortices [10, 13, 16]. The latter can also be created by magnetic dots [17]. Vortex lattice motion, under the action of the Lorentz force, leads to the energy dissipation, and, as a result, to very low critical current J_c . Fluxon confinement (“pinning”), using

various regular pinning arrays [18–22], prevents this motion, and results in an increase of J_c . Therefore, in order to improve J_c , one needs to optimize the pinning of vortices. It has been theoretically predicted [23] and experimentally verified [24, 25] that using quasiperiodic pinning arrays (Penrose lattice), J_c can be enhanced as compared even to periodic or random pinning arrays. By studying — within the GL and London theories — the nucleation of superconductivity and vortex matter in the mesoscopic regime, one can understand, on the one hand, the increase of H_c and J_c , and, on the other hand, one can realize “new functionalities” (e.g., guided flux motion, ratchet effect, fluxon optics, computing using, e.g., cellular automata, etc.) leading to the new field of “fluxonics”.

1.1 Mesoscopic superconductors: a competition between the vortex-vortex interaction and the effect of boundaries

In mesoscopic samples there is competition between the vortex-vortex interaction leading to a triangular vortex lattice, being the lowest-energy configuration in bulk material (and films), and the boundary, which tries to impose its geometry on the vortex lattice. Thus, both the geometry and size of the specimen influence the vortex configurations, due to the interaction between vortices and the surface. Therefore, for small enough samples (with sizes comparable to ξ), the conventional hexagonal lattice predicted by Abrikosov no longer exists, and vortex configurations adjust to the sample geometry, yielding some kind of “vortex molecule” states (see, e.g., [10, 11, 13, 26, 27]). For example, a circular geometry will favor vortices situated on a ring near the boundary, and only far away from the boundary its influence diminishes and the triangular lattice may reappear [26]. Therefore, it is expected that different geometries will favor different arrangements of vortices and will make certain vortex configurations more stable than others [12]. In small systems vortices may overlap so strongly that it is more favorable to form one big giant vortex [28]. As a consequence, it is expected that the giant to multivortex transition will be strongly influenced by the geometry of the boundary as will be also stability of the giant vortex configuration.

1.2 Vortex states in mesoscopic disks

A mesoscopic superconducting disk is the most simple system to study confined vortex matter where the effects of the sample boundary play a crucial role. At the same time, it is a unique system because just by using disks of different radii, or by changing the external parameters, i.e., the applied magnetic field or temperature, one can cover — within the same geometry — a wide range of very different regimes of vortex matter in mesoscopic superconductors.

Early studies of vortex matter in mesoscopic disks were focused on a limiting case of thin disks or disks with small radii in which vortices arrange themselves in rings [5, 6, 29–32] in contrast to infinitely extended superconductors where the triangular Abrikosov vortex lattice is energetically favorable [1, 2, 33]. Several studies were devoted to the questions: i) how the vortices are distributed in disks, ii) which vortex configuration is energetically most favorable, and iii) how the transition between different vortex states occurs. Lozovik and Rakoch [32] analyzed the formation and melting of two-dimensional microclusters of particles with logarithmic repulsive interaction, confined by a parabolic potential. The model was applied, in particular, to describe the behaviour of vortices in small thin (i.e., with a thickness smaller than the coherence length ξ) grains of type II superconductor. Buzdin and Brison [34] studied vortex structures in superconducting disks using the image method, where vortices were considered as point-like “particles”, i.e., within the London approximation. Palacios [35] calculated the vortex configurations in superconducting mesoscopic disks with radius equal to $R = 8.0\xi$, where two vortex shells can become stable. The demagnetization effects were included approximately by introducing an effective magnetic field. Geim *et al.* [36] studied experimentally and theoretically the magnetization of different vortex configurations in superconducting disks. They found clear signatures of first- and second-order transitions between states of the same vorticity. Schweigert and Peeters [6] analyzed the transitions between different vortex states of thin mesoscopic superconducting disks and rings using the nonlinear Ginzburg-Landau (GL) functional. They showed that such transitions correspond to saddle points in the free energy: in small disks and rings — a saddle point between two giant vortex (GV) states, and in larger systems — a saddle point between a multivortex state (MV) and a GV and between two MVs. The shape and the height of the nucleation barrier was investigated for different disk and ring configurations. Kanda *et al.* have studied the magnetic response of a mesoscopic superconducting disk by using the multiple-small-tunnel-junction (MSTJ) method. By comparing the voltages at symmetrical positions, they experimentally determine the type of vortex states: GVS or MVS. They also observed the MVS-MVS and MVS-GVS transitions with a fixed vorticity [37]. Milošević, Yampolskii, and Peeters [38] studied vortex distributions in mesoscopic superconducting disks in an inhomogeneous applied magnetic field, created by a magnetic dot placed on top of the disk. It was shown [27], that such an inhomogeneous field can lead to the appearance of Wigner molecules of vortices and antivortices in the disk.

In the work of Baelus *et al.* [39] the distribution of vortices over different vortex shells in mesoscopic superconducting disks was investigated in the framework of the nonlinear GL theory and the London theory. They found vortex shells and combination of GV and vortex shells for different vorticities L .

Very recently, the first direct observation of rings of vortices in mesoscopic Nb disks was done by Grigorieva *et al.* [40] using the Bitter decoration technique. The formation of concentric shells of vortices was studied for a broad range of vorticities L . From images obtained for disks of different sizes in a range of magnetic fields, the authors of Ref. [40] traced the evolution of vortex states

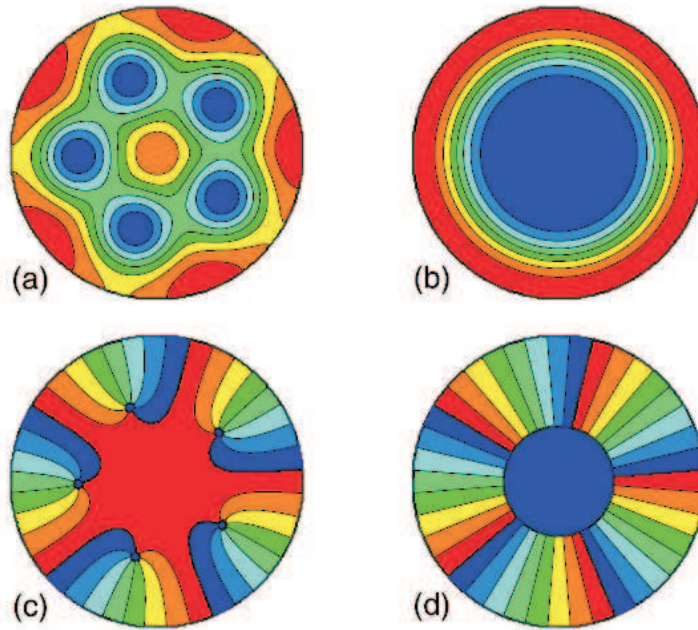


Figure 1.1: The Cooper-pair density for the multivortex state (a) and the giant vortex state (b), and the phase of the order parameter for the multivortex state (c) and the giant vortex state (d) with vorticity $L = 5$ in a superconducting disk with radius $R/\xi = 6.0$. High (low) cooper-pair density is given by red (blue) region. Phases near $2\pi(0)$ are given by red (blue) (After Ref. [41]).

and identified stable and metastable configurations of interacting vortices. Furthermore, the analysis of shell filling with increasing L allowed them to identify magic number configurations corresponding to the appearance of consecutive new shells. Thus, it was found that for vorticities up to $L = 5$ all the vortices are arranged in a single shell. Second shell appears at $L = 6$ in the form of one vortex in the center and five in the second shell [state (1,5)], and the configurations with one vortex in the center remain stable until $L = 8$ is reached, i.e., (1,7). The inner shell starts to grow at $L = 9$, with the next two states having 2 vortices in the center, (2,7) and (2,8), and so on. From the results of the experiment [40] it is clear that, despite the presence of pinning, vortices generally form circular configurations as expected for a disk geometry, i.e., the effect of the confinement dominates over the pinning. Similar shell structures were found earlier in different systems such as vortices in superfluid He [42–45], charged particles confined by a parabolic potential [46], dusty plasma [47], and colloidal particles confined to a disk [48]. Analyzing the size-dependence of the vortex shells formation and studying the crossover from the regime of thin mesoscopic disks to thick macroscopic disks when the effects of London screening are taking into account, Misko *et al.* [8] obtained vortex shell configurations missed in earlier theoretical works and found the regions of their stability, in agreement with the experiment [40]. Very recently, another regime of vortex confinement in disks was studied when the pinning is strong as compared to the confinement [9]. The pinning-induced cluster/giant vortex formation was first experimentally observed [9] in the presence of strong disorder. It was shown that the observed phenomenon is due to the selective enhancement of the pinning strength due to confinement in mesoscopic disks (the cluster/giant vortex formation was not observed in films without disks).

1.3 Symmetry-induced vortex states in mesoscopic superconductors with noncircular geometries

Mesoscopic superconductors with noncircular geometries have attracted a considerable interest due to the opportunity to study the interplay between the circular symmetry of the applied magnetic field and noncircular boundaries. Moshchalkov *et al.* [3] measured the superconducting/normal transition in superconducting lines, squares, and square rings using resistance measurements. Bruyndoncx *et al.* [49] calculated the $H - T$ phase diagram for a square with zero thickness in the framework of the linearized Ginzburg-Landau theory, which is only valid near the superconducting/normal boundary. They compared their results with the $H - T$ phase boundary obtained from resistance measurements. Using the nonlinear Ginzburg-Landau equations, the distributions of the order parameters and magnetic field in square loops with leads attached to it were studied [4]. It was found that the order parameter distribution in the loop is very inhomogeneous, with the enhancement near the corners of the square

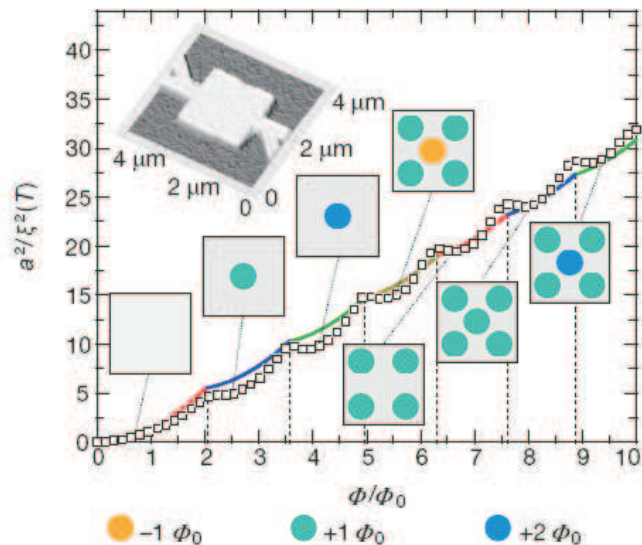


Figure 1.2: Comparison between the calculated (continuous coloured curve) and the measured $T_c(\Phi)$ phase boundary (open squares). The experimental data have been corrected for the presence of the measuring leads. A zero-temperature coherence length $\xi(0) = \xi(T)\sqrt{1-T/T_c} = 99$ nm was used to obtain the best agreement. The zero-field critical temperature is $T_c = 1.36$ K. The top left inset shows the atomic force microscope image of the investigated $2 \times 2 \mu\text{m}^2$ square. In the seven insets, the vortex structure in different regions of the phase diagram is shown schematically with coloured circles. In the range $5 < \Phi/\Phi_0 < 0.63$, an antivortex is formed spontaneously at the centre of the square, coexisting with four Φ_0 -vortices along the diagonals (After Ref. [10]).

loop. Using the criterion of a “superconducting path”, the $H - T$ phase boundary was calculated [4], in agreement with the experiment [3]. Schweigert and Peeters [28, 29], calculated the nucleation field as a function of the sample area for disks, squares, and triangles with zero thickness. Jadallah *et al.* [50] computed the superconducting/normal transition for mesoscopic disks and squares of zero thickness. For macroscopic squares, the magnetic field distribution and the flux penetration are investigated in detail by experimental observations using the magneto-optical Faraday effect and by first-principles calculations that describe the superconductor as a nonlinear anisotropic conductor [51].

The noncircular geometry brings new properties to the vortex matter, which offers unique possibilities to study the interplay between the C_∞ symmetry of the magnetic field and the discrete symmetry of the boundary conditions. Superconductivity in mesoscopic equilateral triangles, squares, etc., in the presence of a magnetic field nucleates by conserving the imposed symmetry (C_3 , C_4) of

the boundary conditions [10] and the applied vorticity. In an equilateral triangle, for example, in an applied magnetic field H generating two flux quanta, $2\Phi_0$, superconductivity appears as the C_3 -symmetric combination $3\Phi_0 - \Phi_0$ (denoted as “3-1”) of three vortices and one antivortex in the center. These symmetry-induced antivortices can be important not only for superconductors but also for symmetrically confined superfluids and Bose-Einstein condensates. Since the order parameter patterns reported in Refs. [10] have been obtained in the framework of the linearized Ginzburg-Landau (GL) theory, this approach is valid only close to the nucleation line $T_c(H)$. In the limit of an extreme type II superconductor ($\kappa \gg 1$), it has been shown that a configuration of one antivortex in the center and four vortices on the diagonals of the square is unstable away from the phase boundary [12, 52]. Such a vortex state is very sensitive to any distortion of the symmetry and can easily be destroyed by a small defect set to the system [53]. Mertelj and Kabanov found the symmetry-induced solution with an antivortex in a thin-film superconducting square [54], in a broader region of the phase diagram than that in Refs. [10]. Possible scenarios of the penetration of a vortex into a mesoscopic superconducting triangle with increasing magnetic field have been studied in Ref. [11]. While a single vortex enters the triangle through a midpoint of one side, a symmetric (“3-2”) combination of three vortices and one antivortex with vorticity $L_{av} = 2$ turns out to be energetically favorable when the vortices are close to the center of the triangle [11]. Misko *et al.* [13] studied the stable vortex-antivortex molecules. Since the interaction between the vortex and antivortex is repulsive in the type-I superconductor, the vortex-antivortex configuration is stable, while in type-II, it is unstable because the sign in the forces of vortex-vortex and vortex-antivortex interaction is changed when passing the dual point $\kappa = 1/\sqrt{2}$, combined with the condensate confinement by the boundaries of the mesoscopic triangle [13].

1.4 Superconductivity in mesoscopic squares and triangles

Comparing with the disk, the vortex patterns in mesoscopic square are quite different. Baelus and Peeters [12] compared the vortex state of superconducting disks, squares, and triangles with the same surface area having nonzero thickness. They found that for given vorticity the vortex lattice is different for the three geometries, i.e., it tries to adjust to the geometry of the sample. For squares and triangles they found magnetic field regions where there is a coexistence between a giant vortex state in the center and several separated vortices in the direction of the sample corners (see Fig. 1.3, 1.4).

The antivortex predicted by the theory [10, 13] remain experimentally undetected, mainly because of their high sensitivity to defects in sample edges [53] and extreme vortex proximity [52]. Those states are undistinguishable from a single multiquanta vortex for conventional techniques such as scanning-tunneling and Hall probe microscopy. Geurts *et al.* [16] discovered that these

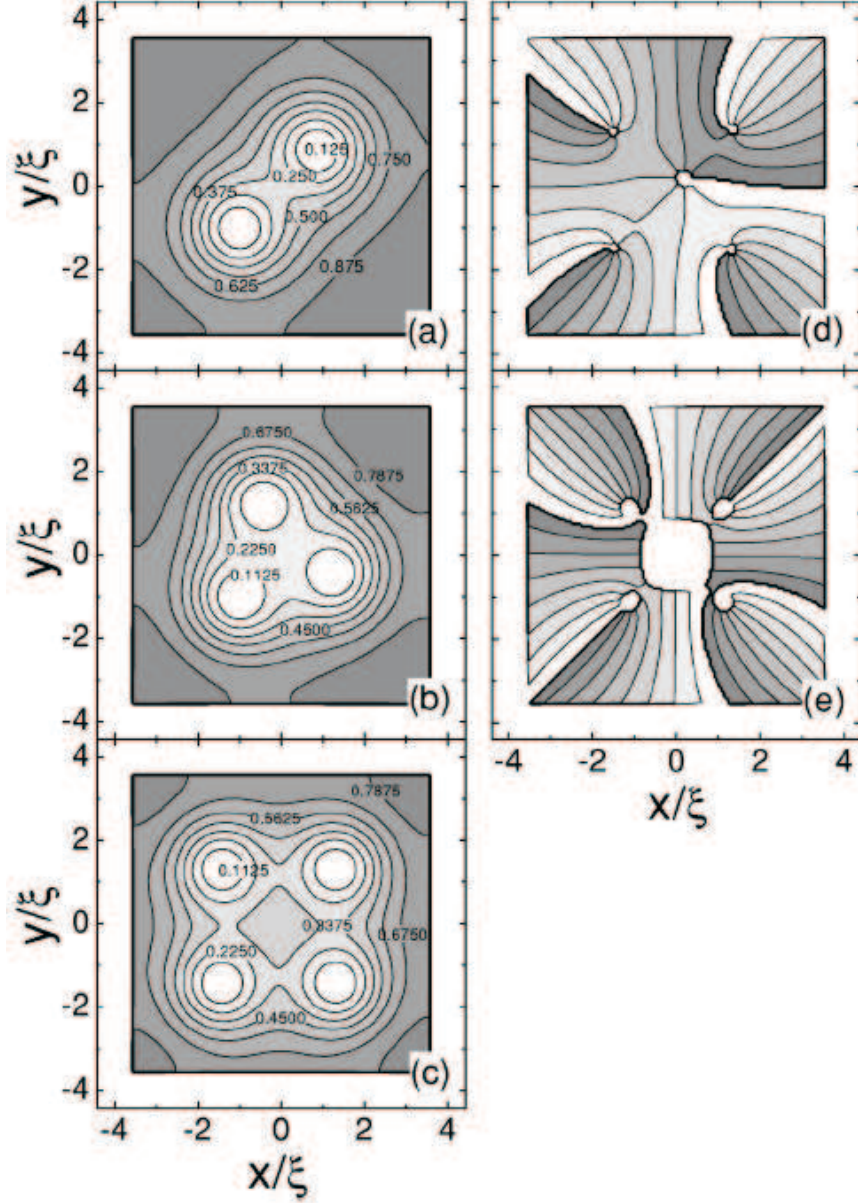


Figure 1.3: (a-c) The Cooper-pair density for a multivortex state in a square with $L = 2, 3$, and 4 at $H_0/H_{c2} = 0.42, 0.67$, and 0.745 , respectively. High Cooper-pair density is given by dark regions, low Cooper-pair density by light regions. (d,e) The phase of the order parameter for the multivortex states with $L = 5$ at $H_0/H_{c2} = 0.82$ and with $L = 6$ at $H_0/H_{c2} = 1.32$. Phases near zero are given by light regions and phases near 2π by dark regions (*After Ref. [12]*)

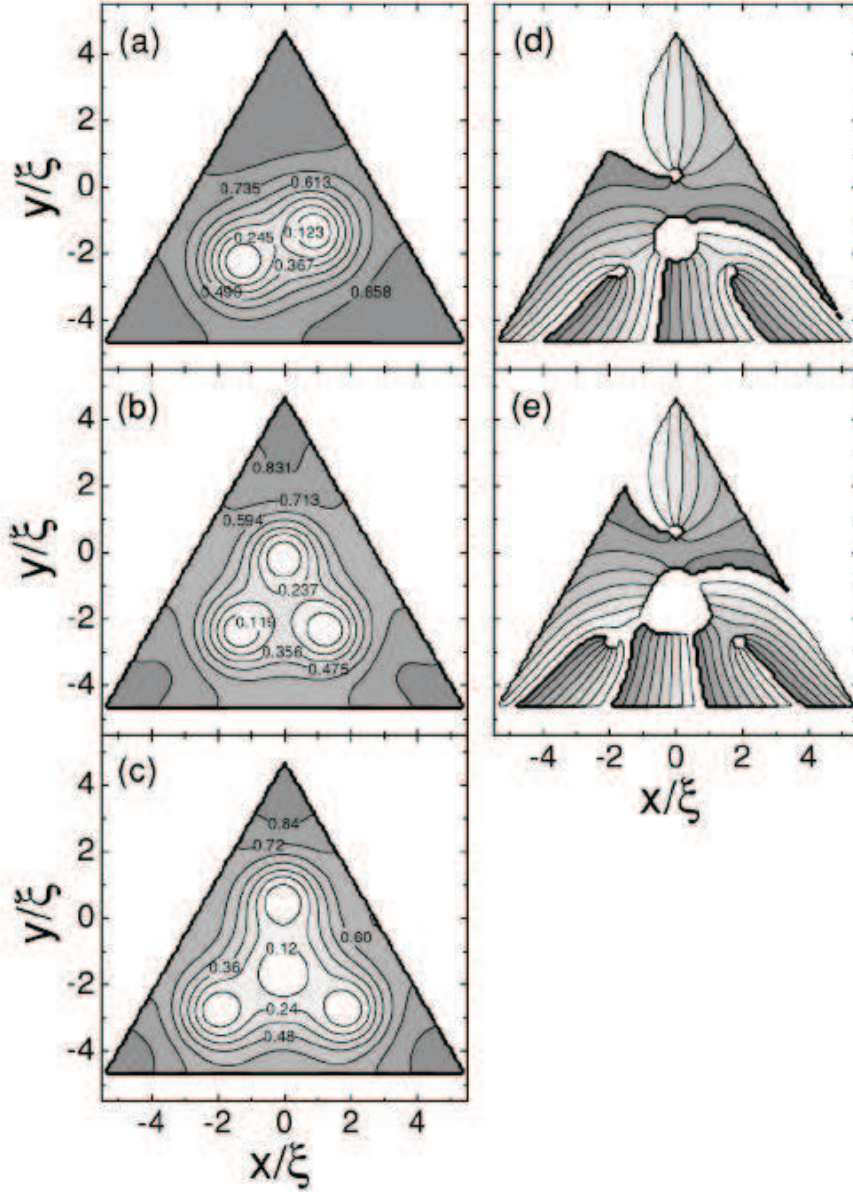


Figure 1.4: (a-c) The Cooper-pair density for a multivortex state in a triangle with $L = 2, 3,$ and 4 at $H_0/H_{c2} = 0.495, 0.82,$ and $0.745,$ respectively. High Cooper-pair density is given by dark regions, low Cooper-pair density by light regions. (d,e) The phase of the order parameter for the multivortex states with $L = 5$ at $H_0/H_{c2} = 1.27$ and with $L = 6$ at $H_0/H_{c2} = 1.345.$ Phases near zero are given by light regions and phases near 2π by dark regions (*After Ref. [12]*).

fascinating (but experimentally not observed so far) states can be enforced by artificial fourfold pinning, with their diagnostic features enhanced by orders of magnitude. The second-order nucleation of vortex-antivortex molecules can be driven by either temperature or an applied magnetic field, with stable asymmetric vortex-antivortex equilibria found on its path.

Up to now, the research of the mesoscopic squares and triangles was mainly done within the Ginzburg-Landau theory. The formation of vortices in rectangles in the case when $\kappa \gg 1$ and the external field $H_{c1} < H \ll H_{c2}$, and the London theory gives a good approximation in the multivortex regime, was done by Sardella *et al.* [55]. They found the free energy with arbitrary vortex configurations in rectangle and mainly discussed the *elongated* rectangles or thin films, where the energy expression takes a relatively simple form. The goal of this thesis is to obtain the multivortex configurations in squares and triangles by using the molecular dynamics simulation.

Chapter 2

Vortex states in rectangles

2.1 Theoretical approach

2.1.1 The London equation

The distribution of the order parameter ψ and the vector potential \mathbf{A} in a superconductor can be found by solving the Ginzburg-Landau equation, which is given by

$$\alpha\psi + \beta|\psi|^2\psi + \frac{1}{2m^*}\left(\frac{\hbar}{i}\nabla - \frac{e^*}{c}\mathbf{A}\right)^2\psi = 0 \quad (2.1)$$

and

$$\mathbf{J} = \frac{c}{4\pi}\text{curl}\mathbf{h} = \frac{e^*\hbar}{2m^*i}(\psi^*\nabla\psi - \psi\nabla\psi^*) - \frac{e^{*2}}{m^*c}\psi^*\psi\mathbf{A}, \quad (2.2)$$

where $e^* = 2e$ and $m^* = 2m_e$ are the charge and mass of a Cooper pair, respectively. However, in most cases, Eqs. (2.1)-(2.2) with various boundary conditions can only be solved numerically. We consider the case of a strong type-II superconductor where the Ginzburg-Landau parameter $\kappa = \lambda/\xi \gg 1$. Since in this case, the density of Cooper pairs heals to a constant in a short distance near the interface of the superconductor state and normal state (the region outside the superconductor and the vortex core), the density can be treated uniform except the core region of the vortex with a radius $r \simeq \xi$ and the region near the surface. Thus, outside those regions, the magnetic field \mathbf{h} is described by the London equation Eq. (2.3):

$$-\lambda^2\nabla^2\mathbf{h} + \mathbf{h} = 0. \quad (2.3)$$

We notice that if this relation is held everywhere, the fluxoid for any path would be zero. This can be corrected by adding a term to take the core into account. Thus, we obtain the modified London equation

$$-\lambda^2\nabla^2\mathbf{h} + \mathbf{h} = \Phi_0\hat{\mathbf{z}}\sum_i\delta(\mathbf{r} - \mathbf{r}_i), \quad (2.4)$$

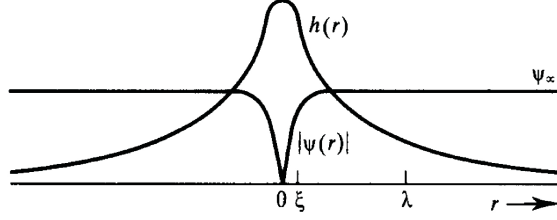


Figure 2.1: Structure of an isolated Abrikosov vortex in a material with $\kappa \approx 8$. The maximum value of $h(r)$ is approximately $2H_{c1}$ (After Ref. [2]).

where $\hat{\mathbf{z}}$ is a unit vector along the vortex, $\delta(\mathbf{r} - \mathbf{r}_i)$ is a two-dimensional δ function, \mathbf{r}_i is super position of the vortex.

One Isolated Abrikosov Vortex

Now we consider a simple case, one vortex is located in a infinite large sample. The London equation is

$$-\lambda^2 \nabla^2 \mathbf{h} + \mathbf{h} = \Phi_0 \hat{\mathbf{z}} \delta(\mathbf{r}). \quad (2.5)$$

This equation has an exact solution,

$$h(r) = \frac{\Psi_0}{2\pi\lambda^2} K_0\left(\frac{r}{\lambda}\right), \quad (2.6)$$

where K_0 is a zeroth order Hankel function of imaginary argument. Qualitatively, $K_0(r/\lambda)$ cuts off as $e^{-r/\lambda}$ at large distances and diverges logarithmically as $\ln(\lambda/r)$ as $r \rightarrow 0$. This divergence is eliminated by a cut off at $r \sim \xi$, where the cooper pair density starts dropping to zero, as shown in Fig. 2.1.

The London free energy per unit volume of the superconducting sample is given by

$$\mathcal{F} = \frac{1}{8\pi A} \int d^2r \{ \mathbf{h}^2 + \lambda^2 |\nabla \times \mathbf{h}|^2 \}. \quad (2.7)$$

Since we have

$$\begin{aligned} |\nabla \times \mathbf{h}|^2 &= (\nabla \times \mathbf{h}) \cdot (\nabla \times \mathbf{h}) \\ &= \nabla \cdot (\mathbf{h} \times \nabla \times \mathbf{h}) + \mathbf{h} \cdot (\nabla \times \nabla \times \mathbf{h}) \\ &= \nabla \cdot (\mathbf{h} \times \nabla \times \mathbf{h}) - \mathbf{h} \nabla^2 \mathbf{h}, \end{aligned} \quad (2.8)$$

we then obtain:

$$\begin{aligned}\mathcal{F} &= \frac{1}{8\pi A} \int d^2r \mathbf{h} \cdot (\mathbf{h} - \lambda^2 \nabla^2 \mathbf{h}) + \frac{\lambda^2}{8\pi A} \int d^2r \nabla \cdot (\mathbf{h} \times \nabla \times \mathbf{h}). \\ &= \frac{1}{8\pi A} \int d^2r |\mathbf{h}| \Phi_0 \sum_i \delta(\mathbf{r} - \mathbf{r}_i) + \frac{\lambda^2}{8\pi A} \oint d\ell \mathbf{h} \times \nabla \times \mathbf{h}.\end{aligned}\quad (2.9)$$

where we have used Eq. (2.19) and Gauss theorem. The integration in Eq. (2.9) excludes the cores of vortices, so the first term contributes nothing and the second term gives contribution in encircling the cores of vortices and also at the sample boundary. For the isolated vortex, we obtain:

$$\epsilon_1 = \frac{\lambda^2}{8\pi} \left[h \frac{dh}{dr} 2\pi r \right]_{\xi}, \quad (2.10)$$

where ϵ_1 is the energy per unit length. Using a approximation

$$K_0(r/\lambda) \approx 0.12 - \ln(r/\lambda), \quad \text{when } \xi \ll r \ll \lambda, \quad (2.11)$$

we arrive at

$$\epsilon_1 = \frac{\phi_0}{8\pi} h(\xi) \approx \frac{\phi_0}{8\pi} h(0), \quad (2.12)$$

where $h(\xi) \approx h(0)$ because the density of Cooper pairs drops to zero when $r \leq \xi$. Using Eq. (2.11) again and dropping the term 0.12 as not significant in view of the approximation made in imposing a cut off at ξ , we finally arrive at

$$\epsilon_1 = \left(\frac{\Phi_0}{8\pi\lambda} \right)^2 \ln \kappa. \quad (2.13)$$

Since this depends only logarithmically on the core size, the result should be quite reliable, despite the crude treatment of the core.

Interaction between Vortex Lines

In the high- κ approximation, it is easy to treat the interaction energy between two vortices. Since in this approximation the medium is linear and we may use superposition of vortices. Thus the field is given by

$$\begin{aligned}\mathbf{h}(\mathbf{r}) &= \mathbf{h}_1(\mathbf{r}) + \mathbf{h}_2(\mathbf{r}) \\ &= [h(|\mathbf{r} - \mathbf{r}_1|) + h(|\mathbf{r} - \mathbf{r}_2|)] \hat{\mathbf{z}},\end{aligned}\quad (2.14)$$

where \mathbf{r}_1 and \mathbf{r}_2 are the coordinates of the two vortices and $h(r)$ is given by Eq. (2.6). The energy can be obtained by substituting this in Eq. (2.9). The result for the increase in free energy per unit length associated with the interaction between the vortex lines can be written

$$\begin{aligned}
\Delta F &= \frac{\Phi_0}{8\pi} [h_1(\mathbf{r}_1) + h_1(\mathbf{r}_2) + h_2(\mathbf{r}_1) + h_2(\mathbf{r}_2)] \\
&= 2 \left[\frac{\Phi_0}{8\pi} h_1(\mathbf{r}_1) \right] + \frac{\Phi_0}{4\pi} h_1(\mathbf{r}_2),
\end{aligned} \tag{2.15}$$

where we use the symmetry properties $h_1(r_1) = h_2(r_2)$ and $h_1(r_2) = h_2(r_1)$. The first term is just the sum of the energies of two individual vortex lines. The second term is the interaction energy that we were looking for

$$F_{12} = \frac{\Phi_0}{4\pi} h_1(\mathbf{r}_2) = \frac{\Phi_0^2}{8\pi^2 \lambda^2} K_0(r_{12}/\lambda). \tag{2.16}$$

As noted earlier, this falls off as $r_{12}^{1/2} e^{-r_{12}/\lambda}$ at large distances and varies logarithmically at small distances. The interaction is repulsive for the usual case, in which the flux has the same direction in both vortices. The force arising from this interaction is obtained by taking a derivative of F_{12} .

$$\mathbf{f}_{12} = \frac{\Phi_0^2}{8\pi^2 \lambda^3} K_1(r_{12}/\lambda) \hat{\mathbf{r}} \tag{2.17}$$

where $\hat{\mathbf{r}} = \mathbf{r}_{12}/r_{12}$ is a unit vector and K_1 is a first order Hankel function of imaginary argument. The vortex can be in static equilibrium at any given position only if the total force from other vortex is zero. This can be accomplished if each vortex is surrounded by a symmetrical array such as square or triangle. However, it turns out that square and any other kind of array except triangular are unstable states, so that the small displacement tend to grow. The triangular array is stable [56]. Unfortunately even the triangular array will feel a force transverse to any transport current, so that the vortices will move unless they are pinned in place by inhomogeneities in the medium. Since flux motion causes energy dissipation and induces a longitudinal resistive voltage, this situation is crucial in determining the usefulness of type II superconductors in the construction of high-field superconducting solenoids, where strong currents and fields inevitably must coexist.

2.1.2 Image technique applied for solving the London equation

Image technique is wildly used to solve differential equations. At the interface of superconductive and nonconductive material, physically the normal current should be forbidden, which gives the boundary condition. For an isolated vortex, it can be satisfied by putting an imaginary antivortex in the nonconductive material (see Fig. 2.2). So we can use this very powerful tool to exactly solve some London equations and obtain analytical results. For the cylindrical symmetry, one vortex has just one image (see Fig. 2.3). Buzdin and Brison [34] found the expression of Gibbs free energy of an arbitrary vortex configuration for the

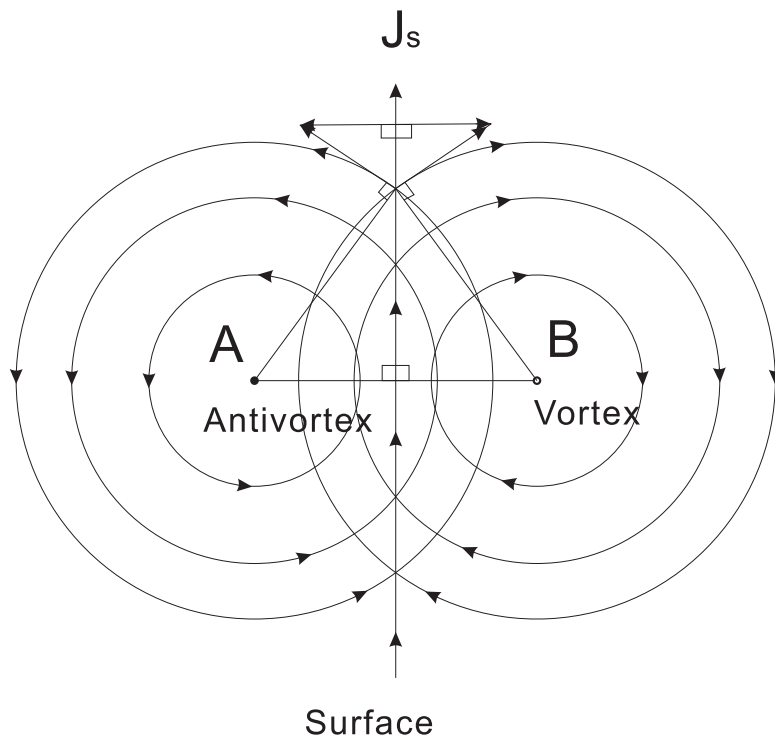


Figure 2.2: The effect of the surface on an isolated vortex at point B is the same as placing an antivortex at the point A. The contribution of the antivortex to the normal current at the surface has the same value as that of the vortex (located at point B), but with the opposite direction. As a result, the total normal current is zero.

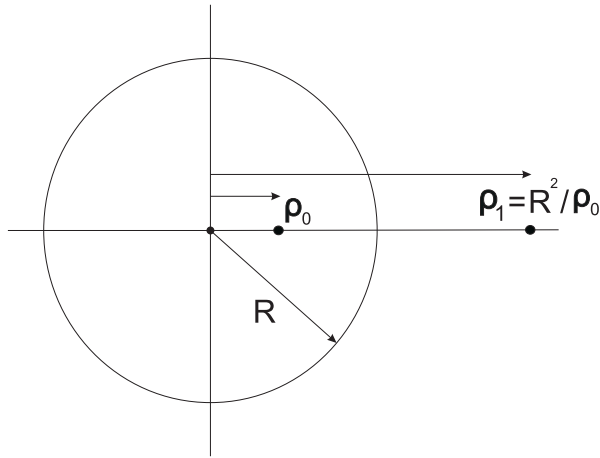


Figure 2.3: Vortex image in a disk. One vortex is situated in a disk of radius R at a distance ρ_0 from disk's center. The image antivortex, we used to satisfy the boundary condition, is located at position ρ_1 outside the disk.

small disk by summing the contribution of all the vortices and antivortices. The position of the image for a cylinder is given by

$$\mathbf{r}_i = \mathbf{r}_0 + \frac{R^2}{|\mathbf{r}_v - \mathbf{r}_0|^2}(\mathbf{r}_v - \mathbf{r}_0), \quad (2.18)$$

where R is the radius of the circle, \mathbf{r}_0 is coordinate of its center, \mathbf{r}_v and \mathbf{r}_i are the positions of the vortex and its image, respectively. So the effect of the circular boundary of the disk is equivalent to placing an antivortex at position \mathbf{r}_i in an infinite superconductor.

For the square, we also investigated the image of the vortex. We found that each vortex has a infinite number of images (see Fig. 2.4). Fortunately, they arrange periodically and since the effect of the vortex-vortex (and also vortex-antivortex) interaction decays exponentially at large distance, and we are only interested in the vortices locating *inside* the square, it is safe to make a cut off at a suitable distance ($\sim 6\lambda$).

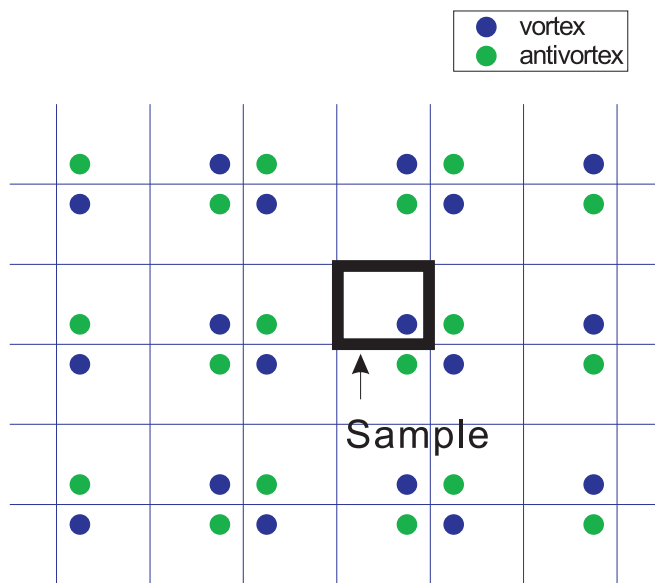


Figure 2.4: Vortex images in a square. The number of the images of a vortex located inside the square sample (the inside region of the thick black lines) is infinite in principle, but since the interaction decays fast ($\sim e^{-r/\lambda}$), it is safe to make a cut off at a suitable distance ($\sim 6\lambda$).

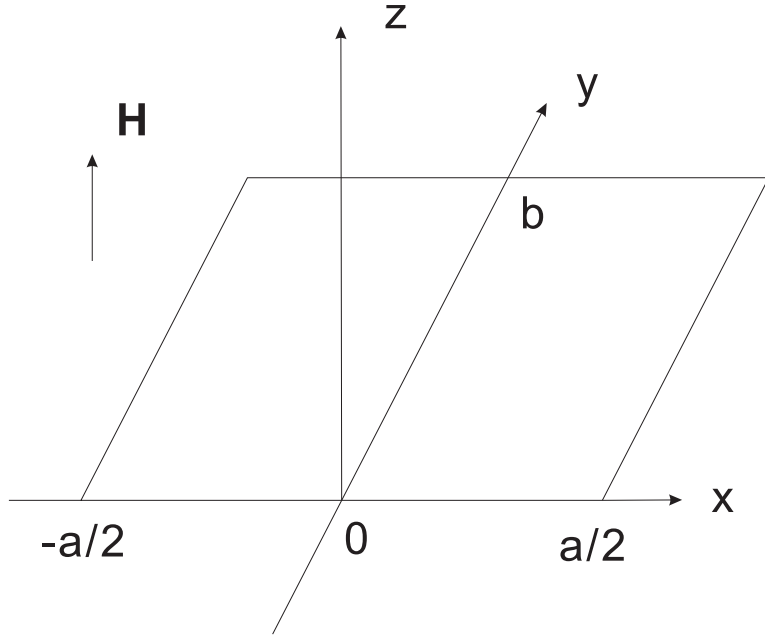


Figure 2.5: The cross-section of a rectangle superconductor with sides a and b . The external magnetic field \mathbf{H} is directed along the z -axis, and its value is assumed to be constant outside the sample.

2.1.3 Solution of the London equation for a rectangle

Green's function is another powerful tool for analyzing the contribution of point sources such as charges or vortex lines in superconductors in the London approximation. Although usually it is more complex than the image method, and sometimes the image method may be used to find the Green's function, it can give an exact result which equals the total contribution of an infinite number of images. For the rectangle problem, cartesian coordinates should be the simplest and the London equation for the local magnetic field $\mathbf{h} = h\mathbf{z}$ is given by

$$-\lambda^2 \nabla^2 h + h = \Phi_0 \sum_i \delta(\mathbf{r} - \mathbf{r}_i), \quad (2.19)$$

where Φ_0 is the quantum flux and $\mathbf{r}_i = (x_i, y_i)$ is the position of the i th vortex. The geometry of the problem is illustrated in Fig. 2.5, where a and b are the lengths of the two sides of the superconductor film. For the London case, the boundary conditions are given by

$$h(\mathbf{r})|_{r \rightarrow \infty} = H \quad (2.20)$$

and

$$j|_n = 0 \quad (2.21)$$

where H is the magnetic field far away from the sample and $j|_n$ means the normal current at the surface. Consider $4\pi\mathbf{j}/c = \nabla \times \mathbf{h}$, Eq. (2.21) can be satisfied by

$$\left(\frac{\partial h}{\partial x}\right)_{y=0,b} = \left(\frac{\partial h}{\partial y}\right)_{x=\pm a/2} = 0. \quad (2.22)$$

Instead of the above two, we use approximate boundary conditions(i.e., we neglect the distortion of the magnetic field outside the sample due to the sample):

$$h(\pm a/2, y) = h(x, 0) = h(x, b) = H. \quad (2.23)$$

The Equation Eq. (2.19) with the boundary conditions Eq. (2.23) have been solved in paper by Sardella *et al.* by using Green's function [55] method. The following derivation is mainly flowing their idea.

The Green's function G associated with the London equation is given by

$$-\lambda^2 \nabla^2 G + G = \delta(x - x')\delta(y - y'), \quad (2.24)$$

and the corresponding boundary conditions are

$$G(\pm a/2, y) = G(x, 0) = G(x, b) = 0. \quad (2.25)$$

Multiplying Eq. (2.19) by G and Eq. (2.24) by h and subtract one from another, we obtain

$$-\lambda^2(G\nabla^2 h - h\nabla^2 G) = G\Phi_0 \sum_i \delta(\mathbf{r} - \mathbf{r}_i) - h\delta(x - x')\delta(y - y'). \quad (2.26)$$

Integrate Eq. (2.26) over the sample area, we arrive at

$$\begin{aligned} & -\lambda^2 \int_{-a/2}^{a/2} dx \int_0^b dy (G\nabla^2 h - h\nabla^2 G) \\ & = \int_{-a/2}^{a/2} dx \int_0^b dy [G\Phi_0 \sum_i \delta(\mathbf{r} - \mathbf{r}_i) - h\delta(x - x')\delta(y - y')]. \end{aligned} \quad (2.27)$$

Using Gauss theorem, that is

$$-\lambda^2 \int_{-a/2}^{a/2} dx \int_0^b dy (G\nabla^2 h - h\nabla^2 G) = -\lambda^2 \oint_{boundary} dl \left(G \frac{\partial h}{\partial n} - h \frac{\partial G}{\partial n} \right),$$

where $\partial/\partial n$ means derivative in the normal direction. Using the boundary conditions Eqs. (2.25) and (2.23), we obtain

$$\begin{aligned}
& -\lambda^2 \oint_{\text{boundary}} dl \left(G \frac{\partial h}{\partial n} - h \frac{\partial G}{\partial n} \right) \\
& = -\lambda^2 \oint_{\text{boundary}} -H \frac{\partial G}{\partial n} \\
& = \lambda^2 H \int_{-a/2}^{a/2} dx \int_0^b dy \nabla^2 G \\
& = -H \int_{-a/2}^{a/2} dx \int_0^b dy \left[\delta(x-x') \delta(y-y') - G \right] \\
& = -H \left[1 - \int_{-a/2}^{a/2} dx \int_0^b dy G(x, y, x', y') \right],
\end{aligned}$$

and the right-hand part of Eq. (2.27) is

$$\begin{aligned}
& \int_{-a/2}^{a/2} dx \int_0^b dy \left[G \Phi_0 \sum_i \delta(\mathbf{r} - \mathbf{r}_i) - h \delta(x-x') \delta(y-y') \right] \\
& = \Phi_0 \sum_i G(x_i, y_i, x', y') - h(x', y').
\end{aligned}$$

Finally, the magnetic field is given by

$$h(x', y') = H \left[1 - \int_{-a/2}^{a/2} dx \int_0^b dy G(x, y, x', y') \right] + \Phi_0 \sum_i G(x_i, y_i, x', y'). \quad (2.28)$$

The solution for the local magnetic field is thus reduced to the determination of Green's function $G(x, y, x', y')$. In order to do this, first of all, we expand G in a Fourier series

$$G(x, y, x', y') = \frac{2}{b} \sum_{m=1}^{\infty} \sin\left(\frac{m\pi y'}{b}\right) \sin\left(\frac{m\pi y}{b}\right) g_m(x, x'). \quad (2.29)$$

Note that the boundary conditions at $y = 0, b$ are satisfied. Inserting this equation into Eq. (2.24), we obtain

$$\begin{aligned}
& -\lambda^2 \frac{2}{b} \sum_{m=1}^{\infty} \left[\frac{\partial^2 g_m(x, x')}{\partial x^2} \sin\left(\frac{m\pi y'}{b}\right) \sin\left(\frac{m\pi y}{b}\right) \right. \\
& \quad - \left(\frac{m\pi}{b}\right)^2 g_m(x, x') \sin\left(\frac{m\pi y'}{b}\right) \sin\left(\frac{m\pi y}{b}\right) \\
& \quad \left. + \sin\left(\frac{m\pi y'}{b}\right) \sin\left(\frac{m\pi y}{b}\right) g_m(x, x') \right] \\
& = \delta(x-x') \frac{2}{b} \sum_{m=1}^{\infty} \sin\left(\frac{m\pi y'}{b}\right) \sin\left(\frac{m\pi y}{b}\right), \quad (2.30)
\end{aligned}$$

where we used the δ -function representation

$$\delta(y - y') = \frac{2}{b} \sum_{m=1}^{\infty} \sin\left(\frac{m\pi y'}{b}\right) \sin\left(\frac{m\pi y}{b}\right).$$

Since the sequence

$$\left\{ \sqrt{\frac{2}{b}} \sin\left(\frac{m\pi y}{b}\right), m = 1, 2, 3, \dots \right\}$$

is a complete set of orthonormal functions, we obtain

$$-\lambda^2 \frac{\partial^2 g_m(x, x')}{\partial x^2} + \alpha_m^2 g_m(x, x') = \delta(x - x'). \quad (2.31)$$

Here,

$$\alpha_m = \left[1 + \lambda^2 \left(\frac{m\pi}{b} \right)^2 \right]^{1/2}. \quad (2.32)$$

The functions $g_m(x, x')$ must

satisfy the boundary conditions that is $g_m(\pm a/2, x') = 0$. Taking Fourier transform of Eq. (2.31), we get

$$-\lambda^2 (i\omega)^2 F(\omega) + \alpha_m^2 F(\omega) = \frac{1}{2\pi} e^{-i\omega x'},$$

and we express $F(\omega)$

$$F(\omega) = \frac{e^{-i\omega x'}}{2\pi(\lambda^2 \omega^2 + \alpha_m^2)}.$$

Then we get a particular solution to the Eq. (2.31)

$$\begin{aligned} g_m|_{a \rightarrow \infty} &= \frac{1}{2\alpha_m \lambda} e^{-\alpha_m |x - x'|/\lambda} \\ &= \frac{1}{2\alpha_m \lambda} [\cosh(\alpha_m(x - x')/\lambda) - \sinh(\alpha_m|x - x'|/\lambda)]. \end{aligned}$$

The general solution of Eq. (2.31) is:

$$\begin{aligned} g_m &= \frac{1}{2\alpha_m \lambda} [\cosh(\alpha_m(x - x')/\lambda) - \sinh(\alpha_m|x - x'|/\lambda)] \\ &+ A(x') \sinh(\alpha_m x/\lambda) + B(x') \cosh(\alpha_m x/\lambda) \\ &= \frac{1}{2\alpha_m \lambda} [-\sinh(\alpha_m|x - x'|/\lambda) + C(x') \sinh(\alpha_m x/\lambda) + D(x') \cosh(\alpha_m x/\lambda)]. \end{aligned}$$

$C(x')$ and $D(x')$ can be determined using the boundary condition Eq. (2.25), and we find

$$\begin{aligned} C(x') &= -\coth(\alpha_m a/2\lambda) \sinh(x'); \\ D(x') &= \tanh(\alpha_m a/2\lambda) \cosh(x'). \end{aligned}$$

Then the solution for $g_m(x, x')$ is given by

$$g_m(x, x') = \frac{1}{2\lambda\alpha_m \sinh(\alpha_m a/\lambda)} \left\{ \cosh [\alpha_m(|x-x'|-a)/\lambda] - \cosh [\alpha_m(x+x')/\lambda] \right\}. \quad (2.33)$$

Finally, we obtain the expression for the Green's function, which is

$$G(x, y, x', y') = \frac{2}{b} \sum_{m=1}^{\infty} \sin\left(\frac{m\pi y'}{b}\right) \sin\left(\frac{m\pi y}{b}\right) \frac{1}{2\lambda\alpha_m \sinh(\alpha_m a/\lambda)} \times \left\{ \cosh [\alpha_m(|x-x'|-a)/\lambda] - \cosh [\alpha_m(x+x')/\lambda] \right\}. \quad (2.34)$$

Up to now, our results of this section coincide with the results of paper by Sardella *et al.*. However, when taking the integral in Eq. (2.28) they made a mistake, our result is

$$\int_{-a/2}^{a/2} dx \int_0^b dy G(x, y, x', y') = \frac{4}{b} \sum_{m=0}^{\infty} \alpha_{2m+1}^{-2} \frac{b}{(2m+1)\pi} \times \sin\left[\frac{(2m+1)\pi y'}{b}\right] \left[1 - \frac{\cosh(\alpha_{2m+1} x'/\lambda)}{\cosh(\alpha_{2m+1} a/2\lambda)}\right] \quad (2.35)$$

Using the summation formula [57],

$$\begin{aligned} \sum_{l=-\infty}^{+\infty} \frac{\cos(l\pi x)}{(l\pi)^2 + c^2} &= \frac{\cosh[c(1-|x|)]}{c \sinh c} \\ &= 1/c \sum_{m=-\infty}^{+\infty} \exp(-c|x-2m|) \end{aligned} \quad (2.36)$$

we have

$$\begin{aligned} \frac{4}{b} \sum_{m=0}^{\infty} \alpha_{2m+1}^{-2} \frac{b}{(2m+1)\pi} \sin\left[\frac{(2m+1)\pi y'}{b}\right] \\ = \int_0^b dy g(y, y') = 1 - \frac{\cosh[(y'-b/2)/\lambda]}{\cosh(b/2\lambda)}, \end{aligned} \quad (2.37)$$

where

$$\begin{aligned} g(y, y') &= \sum_{m=1}^{\infty} \alpha_m^{-2} \sin\left(\frac{m\pi y'}{b}\right) \sin\left(\frac{m\pi y}{b}\right) \\ &= \frac{1}{2\lambda \sinh(b/\lambda)} \left\{ \cosh [(|y-y'|-b)/\lambda] - \cosh[(y+y')/\lambda] \right\}, \end{aligned} \quad (2.38)$$

So we can simplify the solutions and finally get the expression for the local magnetic field

$$h(x, y) = \Phi_0 \sum_i G(x_i, y_i, x, y) + H \left\{ \frac{\cosh[(y - b/2)/\lambda]}{\cosh(b/2\lambda)} + \frac{4}{b} \sum_{m=0}^{\infty} \alpha_{2m+1}^{-2} \frac{b}{(2m+1)\pi} \sin \left[\frac{(2m+1)\pi y}{b} \right] \frac{\cosh(\alpha_{2m+1} x/\lambda)}{\cosh(\alpha_{2m+1} a/2\lambda)} \right\}. \quad (2.39)$$

Using Eq. (2.9), we obtain the expression for the free energy, that is

$$\mathcal{F} = \frac{\Phi_0}{8\pi A} \sum_i h(x_i, y_i) + \frac{\lambda^2 H}{8\pi A} \left\{ \int_0^b dy \left[\left(\frac{\partial h}{\partial x} \right)_{x=a/2} - \left(\frac{\partial h}{\partial x} \right)_{x=-a/2} \right] + \int_{-a/2}^{a/2} dx \left[\left(\frac{\partial h}{\partial y} \right)_{y=b} - \left(\frac{\partial h}{\partial y} \right)_{y=0} \right] \right\}. \quad (2.40)$$

By integrating the London equation (2.19) we can exactly get the second term of Eq. (2.40). The result is

$$\mathcal{F} = \frac{\Phi_0}{8\pi A} \sum_i h(x_i, y_i) + \frac{HB}{8\pi} - N \frac{\Phi_0 H}{8\pi A}, \quad (2.41)$$

where $A = a \cdot b$ is the sample's area and B is the spatial average of the local magnetic field. Integrating Eq. (2.28) over the area of the superconducting film, one has

$$\begin{aligned} AB &= \int d^2r h(x, y) \\ &= N\Phi_0 - \Phi_0 \sum_i \left\{ \frac{\cosh[(y_i - b/2)/\lambda]}{\cosh(b/2\lambda)} + \frac{4}{b} \sum_{m=0}^{\infty} \alpha_{2m+1}^{-2} \frac{b}{(2m+1)\pi} \sin \left[\frac{(2m+1)\pi y_i}{b} \right] \frac{\cosh(\alpha_{2m+1} x_i/\lambda)}{\alpha_{2m+1} a/\lambda} \right\} \\ &\quad + HA \left\{ \frac{\tanh(b/2\lambda)}{b/2\lambda} - \frac{8}{\pi^2} \sum_{m=0}^{\infty} \frac{\tanh(\alpha_{2m+1} a/2\lambda)}{[(2m+1)\alpha_{2m+1}]^2 (\alpha_{2m+1} a/2\lambda)} \right\}. \end{aligned} \quad (2.42)$$

Usually the Gibbs free energy is needed to study the most stable configuration of the vortex lattice. The Gibbs free energy is given by $\mathcal{G} = \mathcal{F} - BH/4\pi$. From

Eqs. (2.41) and (2.42), we finally arrive at

$$\begin{aligned}
\mathcal{G} &= \frac{\Phi_0^2}{8\pi A} \sum_{i,j} G(x_i, y_i, x_j, y_j) + \frac{\Phi_0 H}{4\pi A} \left\{ \frac{\cosh[(y-b/2)/\lambda]}{\cosh(b/2\lambda)} \right. \\
&\quad + \frac{4}{b} \sum_{m=0}^{\infty} \alpha_{2m+1}^{-2} \frac{b}{(2m+1)\pi} \sin \left[\frac{(2m+1)\pi y}{b} \right] \frac{\cosh(\alpha_{2m+1} x/\lambda)}{\cosh(\alpha_{2m+1} a/2\lambda)} \left. \right\} \\
&\quad - \frac{H^2}{8\pi} \left\{ \frac{\tanh(b/2\lambda)}{b/2\lambda} - \frac{8}{\pi^2} \sum_{m=0}^{\infty} \frac{\tanh(\alpha_{2m+1} a/2\lambda)}{[(2m+1)\alpha_{2m+1}]^2 (\alpha_{2m+1} a/2\lambda)} \right\} \\
&\quad - N \frac{\Phi_0 H}{4\pi A} \tag{2.43}
\end{aligned}$$

The last two terms are the energies associated with the external magnetic field and the vortex cores, respectively. The Green's function in the first term describes the repulsive interaction between vortices and attractive interaction between the vortices and their images which are virtually placed outside the sample. The second term represents the interaction between the i th vortex and the shielding currents. In paper by Sardella *et al.* [55], they worked in the limit of thin film, where $(\pi\lambda/b)^2 \gg 1$ and the term 1 in Eq. (2.32) can be neglected. We notice that Eq. (2.43) can be applied to rectangles with any aspect ratio.

The London theory has a singularity for the vortex self-interaction. We notice that when $i = j$ the Green's function does not converge. So we need to apply a cutoff procedure (see, e.g. [33, 34, 58]), which means a replacement of $|\mathbf{r}_i - \mathbf{r}_j|$ by $a\xi$ for $i = j$. As shown in Ref. [26], the vortex size is $\sqrt{2}\xi$, which means we should take $a = \sqrt{2}$. But in our case, the result is associated with $|x_i - x_j|$ and $|y_i - y_j|$. As an approximation, we take $|x_i - x_j| = |y_i - y_j| = \xi$. The force felt by each vortex can be obtained by taking the derivative of the energy, $F = -\nabla_i V$:

$$\mathbf{F}_i = \sum_{j \neq i} \mathbf{F}_{ij} + \mathbf{F}_{self}^i + \mathbf{F}_M^i \tag{2.44}$$

where

$$\begin{aligned}
F_{x_{ij}} &= f_0 \frac{\lambda}{b} \sum_{m=1}^{\infty} \frac{1}{2} \left[\cos \frac{m\pi}{b} (y_i + y_j) - \cos \frac{m\pi}{b} (y_i - y_j) \right] \frac{1}{\sinh(\alpha_m a/\lambda)} \\
&\quad \times \left\{ \sinh[\alpha_m (|x_i - x_j| - a)/\lambda] \cdot \theta(x_i - x_j) - \sinh[\alpha_m (x_i + x_j)/\lambda] \right\} \tag{2.45}
\end{aligned}$$

and

$$\begin{aligned}
F_{y_{ij}} &= f_0 \frac{\lambda^2}{b} \sum_{m=1}^{\infty} \frac{m\pi}{2b} \left[\sin \frac{m\pi}{b} (y_i + y_j) - \sin \frac{m\pi}{b} (y_i - y_j) \right] \frac{1}{\sinh(\alpha_m a/\lambda)} \\
&\quad \times \left\{ \cosh[\alpha_m (|x_i - x_j| - a)/\lambda] - \cosh[\alpha_m (x_i + x_j)/\lambda] \right\} \tag{2.46}
\end{aligned}$$

are the x- and y-components of the force acting on the i th vortex, which is given by the j th vortex and all its images;

$$F_{x_{self}}^i = f_0 \frac{\lambda}{b} \sum_{m=1}^{\infty} \left[\cos \frac{2m\pi}{b} y_i - \cos \frac{m\pi}{b} \xi \right] \frac{\sinh(2\alpha_m x_i / \lambda)}{\sinh(\alpha_m a / \lambda)} \quad (2.47)$$

and

$$F_{y_{self}}^i = f_0 \frac{\lambda^2}{b} \sum_{m=1}^{\infty} \sin\left(\frac{2m\pi}{b} y_i\right) \frac{1}{\sinh(\alpha_m a / \lambda)} \frac{m\pi}{b} \times \left\{ \cosh[\alpha_m(\xi - a)/\lambda] - \cosh[\alpha_m 2x_i / \lambda] \right\} \quad (2.48)$$

are given by the interaction of the i th vortex and its images; \mathbf{F}_M is the force caused by the Meissner shielding current, which is proportional to the external magnetic field. It is given by

$$F_{x_M}^i = f_0 \frac{H}{Hc_2} \cdot \frac{4\lambda^2}{\pi\xi^2} \sum_{m=0}^{\infty} \frac{\sin\left[\frac{(2m+1)\pi}{b} y\right] \sinh(\alpha_{2m+1} x / \lambda)}{\alpha_{2m+1} (2m+1)\pi \cosh(\alpha_{2m+1} a / 2\lambda)} \quad (2.49)$$

and

$$F_{y_M}^i = f_0 \frac{H}{Hc_2} \cdot \frac{\lambda^2}{\pi\xi^2} \left\{ \frac{\sinh[(y - b/2)/\lambda]}{\cosh(b/2\lambda)} + \frac{4\lambda}{b} \sum_{m=0}^{\infty} \frac{\cos\left[\frac{(2m+1)\pi}{b} y\right] \cosh(\alpha_{2m+1} x / \lambda)}{\alpha_{2m+1}^2 \cosh(\alpha_{2m+1} a / 2\lambda)} \right\}. \quad (2.50)$$

In Eqs. (2.45)-(2.50), $f_0 = \frac{\Phi_0^2}{8\pi A} \frac{1}{\lambda^3}$ is the unit of force. For the stable states, the total force which acts on each vortex should be zero. The molecular dynamic simulation provides a way to find the favorable configurations.

2.2 Numerical results

The solutions of the London equation for a square we found in previous section make it possible to obtain the energy distributions. By taking the derivative with respect to the coordinate, we obtain the total force acting on each vortex at any position in the sample. This allows us to perform the Molecular Dynamics simulation of moving vortices which relax to their stable configurations. It is convenient to express the lengths in unit of λ , the fields in unit of H_{c2} , the energies per unit length in unit of $g_0 = \Phi_0^2/8\pi A \cdot 1/\lambda^2$ and force per unit length in unit of $f_0 = \Phi_0^2/8\pi A \cdot 1/\lambda^3$, where A is the sample's area.

2.2.1 The free energy distribution

From Eq. (2.43), we see that the free energy include five terms. The last two terms which are associated with the external magnetic field and the vortex cores, respectively are constant (i.e., do not depend on x and y). Only the first three terms vary with position, and we are interested in analyzing these terms in order to find the energetically favorable vortex states. The second term is proportional to the external magnetic field. More precisely, it is proportional to the field penetrating from the external field, which is caused by Meissner effect. The Meissner state is shown in Fig. 2.6 (a). This term is nothing else but just the field times a constant. As we expected, this field distribution is minimum at the center. Thus, the Meissner screening current is always trying to push the vortex into the center, that is why more vortices can be introduced by increasing the external magnetic field in reality.

The first term include two contributions. One comes from the interaction between the vortex and its own image. The other one comes from the interaction between two vortices and their images. The interaction between the vortex and image is attractive, or in other words, the vortex is attracted by the surface. So the critical boundary condition (no normal current) is always trying to pull the vortex out of the sample. It costs energy to push the vortex from the boundary to the center. This self-energy is shown in Fig. 2.6 (b). The attractive self energy and the repulsive Meissner energy form the well know surface (Bean-Livingston) barrier. As shown in Fig. 2.6 (c), the confinement energy distribution near the first critical field shows the barrier near the surface. And we can also see that the barrier near the corner is much higher than that near the midpoint of the edges, so the first vortex tend to enter the sample through one of the four midpoint of the edges. The interaction between two vortices is repulsive. When one vortex is located in the sample, it is always trying to push other vortices away from itself as far as possible. And also its images attracts other vortices which means the attractive effect of the surface is enhanced and the external magnetic field must increase in order to introduce more vortices into the sample, and also energetically favorable configurations are needed to lower the energy. In Fig. 2.6, one vortex is located in the center, we see that it is really hard for other vortex to enter the sample. By increasing the magnetic field, new vortex can be introduced. And the initial position of the vortices should change. As

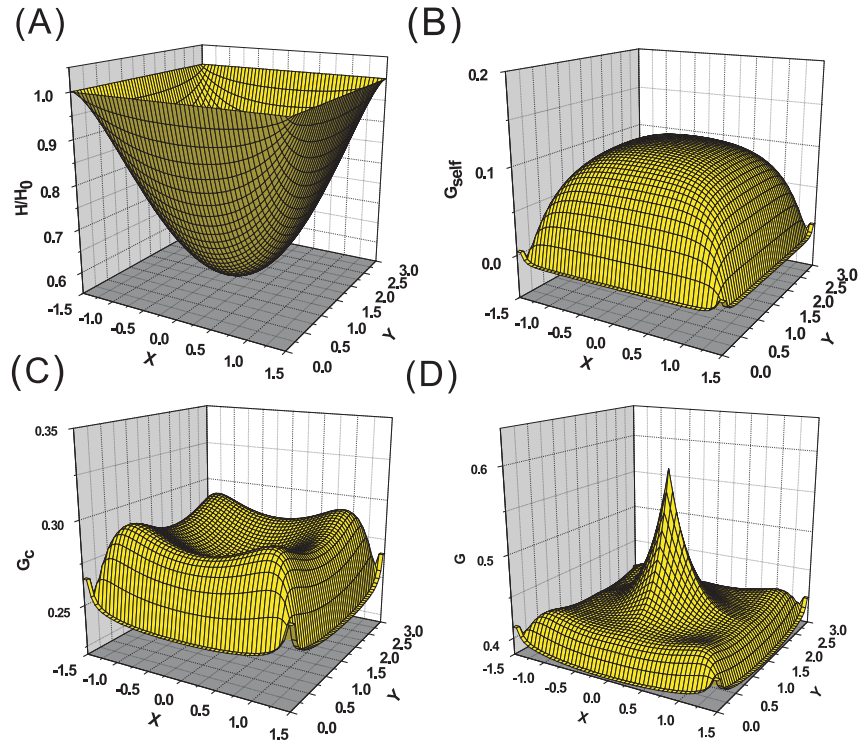


Figure 2.6: (A) The magnetic field distribution in a superconducting square with the length of the side $a = 3\lambda$. H_0 is the external magnetic field. (B) The self-energy distribution shows the attractive effect of the surface. (C) Confinement energy when the external field $H_0 = 0.023H_{c2}$ shows the surface barrier. (D) The free energy distribution when $H_0 = 0.036H_{c2}$ and one vortex is located in the center. $G(x,y)$ is the confinement energy, which is equal to the free energy increase by adding a vortex. The high peak at the core of the vortex shows the repulsive interaction between vortices.

we see that even we apply a magnetic field that is large enough to support two or more vortices in the sample, if one vortex is initially located in the center, the barrier is still too high to let in other vortices. So the transition from the $L = 1$ state to the $L = 2$ state is accompanied. Not that the symmetry of a mesoscopic sample plays an important role in transition between states with different vorticity L . For instance, the $L = 1$ to $L = 2$ transition in a square breaks the C_4 -symmetry of the initial state $L = 1$ may occur as a jump to some other states such as $L = 5$ when the external field is large enough. In this case, the initial C_4 -symmetry preserves also for the final state $L = 5$ (i.e., vortices enter symmetrically though the midpoints of the square). Depending on the sample's size and material (κ) and external parameters (H, T), one of the possible scenarios of vortex penetration is realized. As we notice, the size of the square is also important for the vortex states. In Fig. 2.7 A and B, we show the confinement energy profile of two squares with the length of side $a_1 = 3\lambda$ and $a_2 = 15\lambda$, respectively. For the mesoscopic squares, all the vortices in the sample feel the influence of the screening current, which extends inside the sample while for the microscopic squares, only the ones near the boundary feel the effect of the surface since the screening current dropped almost to zero for distances [8]. And also, for the large squares with low vorticity, the vortices are well separated and the influence of the nearest neighbors is important. They act more like isolated vortices. But for the small ones, the vortices overlap strongly, all the vortices can feel the influence from other vortices. In Fig. 2.7 C, and D, three vortices are located in the sample, respectively. G is the energy required to put one vortex at that point, which is proportional to the magnetic field at the point. We see that the vortex is almost isolated for large square and overlap each other strongly for the small ones. The high peak structures near the core of the vortex are not reasonable. But in reality, since the Cooper pairs' density dropped to zero, those region are actually normal. And also the vortices in stable states never run to those regions as it costs more energy. Those regions as well as the ones very close to the boundary are unimportant, and a suitable cutoff is acceptable.

2.2.2 Vortex patterns in square samples

Eqs. (2.47)-(2.50) provide us with the conditions to use the Molecular Dynamic simulation. We perform our simulation by numerically integrating the overdamped equations of motion

$$\eta \mathbf{v}_i = \mathbf{F}_i = \sum_{j \neq i} \mathbf{F}_{ij} + \mathbf{F}_{self}^i + \mathbf{F}_M^i + \mathbf{F}_T^i. \quad (2.51)$$

η is the viscosity, which is set here to unity. Comparing with Eq. (2.44), we added a thermal stochastic term \mathbf{F}_T^i to simulate the process of annealing in experiment. This temperature contribution should obey the following conditions:

$$\langle F_i^T(t) \rangle = 0 \quad (2.52)$$

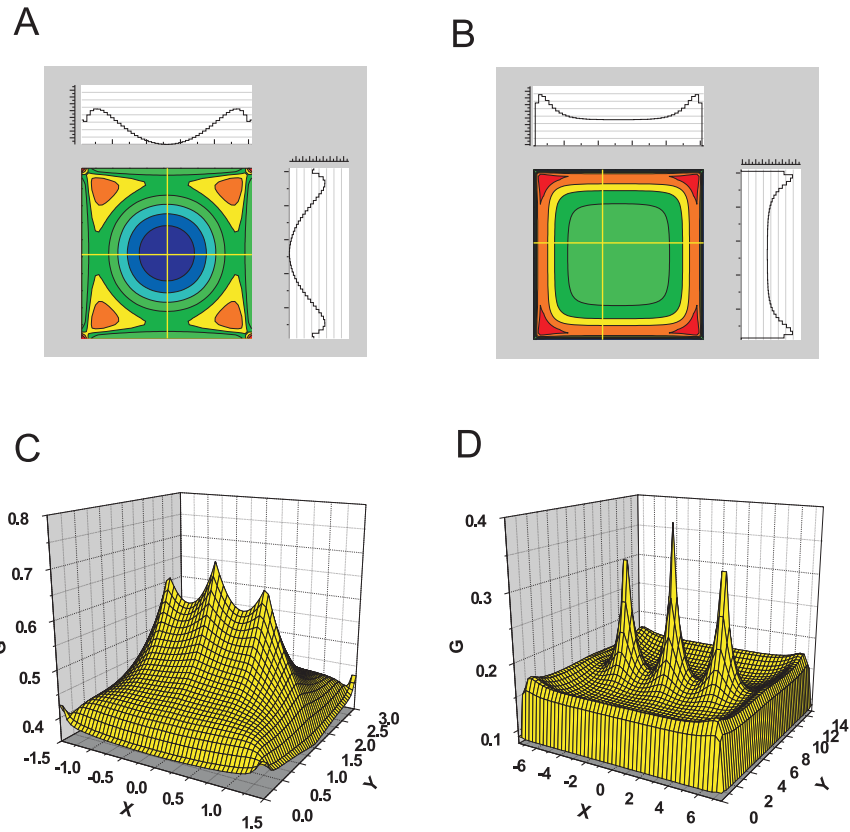


Figure 2.7: A and B are the profile of the confinement energy for $a = 3\lambda$ and 15λ , respectively. C and D show the distribution of the energy in squares with $a = 3\lambda$ and 15λ , respectively. Three vortices are located at $(\pm a/4, a/2)$ and $(0, a/2)$. $G(x,y)$ is the increase of the free energy by adding a vortex at the point (x,y) .

and

$$\langle F_i^T(t)F_i^T(t') \rangle = 2\eta k_B T \delta_{ij} \delta(t - t'). \quad (2.53)$$

The procedure is as follows: first, give each vortex a random position and set a high value for the temperature. Second, calculate the force of each vortex and move them to the new positions. After processing the second step many times, the temperature is gradually decreased to zero. Thus, we obtain the stable states when the total force on each vortex is small enough. If one vortex is kicked out of the sample, we then increase the external magnetic field and return to the first step. we successfully obtained the vortex patterns in square samples with different vorticities. From $L = 1$ to 4 the vortex configurations evolve with increasing applied field as follows (see Fig. 2.8): starting from a Meissner state with no vortex, then one vortex appears in the center, then two locate symmetrically along the diagonal line. Further increasing of the magnetic field leads to the formation of equilateral triangle sharing a symmetry axis with the square, which is the diagonal line. For $L = 4$ it forms perfect square. When $L = 5$, they tend to form either a pentagon or a perfect square with one in the center. As we will discuss later, the second one is more stable. Since the triangle and the pentagon have different symmetry with square, antivortex may be introduced to lower the energy [10]. When $L = 6$, a pentagon with one vortex near the center is formed. Comparing with this configuration in disk, since the asymmetric influence of the boundary, the pentagon is not regular and the one near the center moves close to the side that has two vortices. But for $L = 7$, a regular hexagon is formed, and two symmetry axes are shared with the square. For $L = 8, 15$, comparing with $L = 4, 9, 16$ which form square lattices, there is one vortex missing in one line, which tends to locate near the center, the configuration in this region more like a triangular lattice. Thus, we obtain a kind of “domain structure” where a square and triangular vortex lattices coexist in one sample. For $L = 10, 11, 12$, eight vortices form a *shell* near the boundary, and the number of vortices near the center increases from two to four. Also for $L = 17, 18, 19$, twelve vortices form a shell, and the rest form a structure almost the same as $L = 5, 6, 7$, respectively. What is more interesting, there are two stable states for $L = 5$. For $L = 17$, the five vortices can also form these two possible states, which cause two stable states for $L = 17$ (see Fig 2.11). When more vortices are introduced, the average distance between the vortices decreases. So the interaction between the vortices becomes more and more important which means more triangular lattice should be formed. As discussed above, for $L = 25$, the configuration should arrange in a square lattice, but actually, it is distorted which is trying to evolve to the triangular lattice which is more stable. The square shell is also not as stable as for small vorticity L . More and more triangular-lattice “domains” are formed for large vorticities.

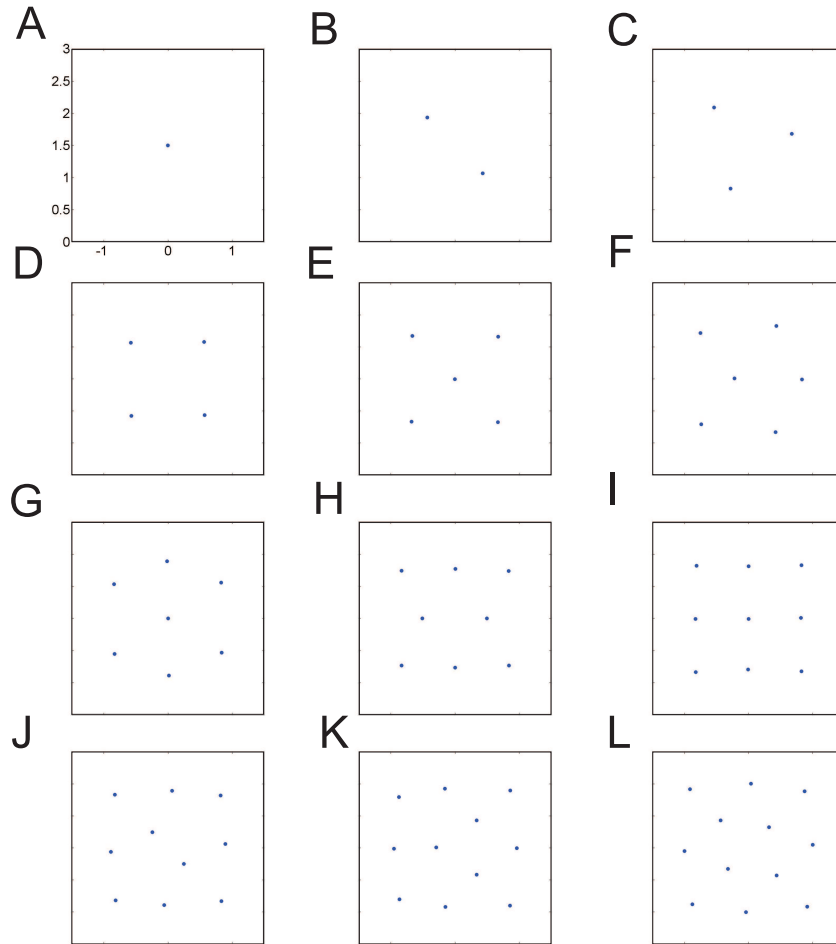


Figure 2.8: $A \sim L$ show the vortex configurations for vorticity L varied from 1 to 12, respectively. The sample tries to impose its square geometry on the lattice while the vortex-vortex interaction tries to form triangular lattice which is energetically favorable in an infinite superconductor. As a result, for $L = 1, 4, 9$, perfect square lattice is formed. For $L = 7$ and 8 , perfect triangular lattice is formed. All the states are trying to share the symmetry axis with the sample.

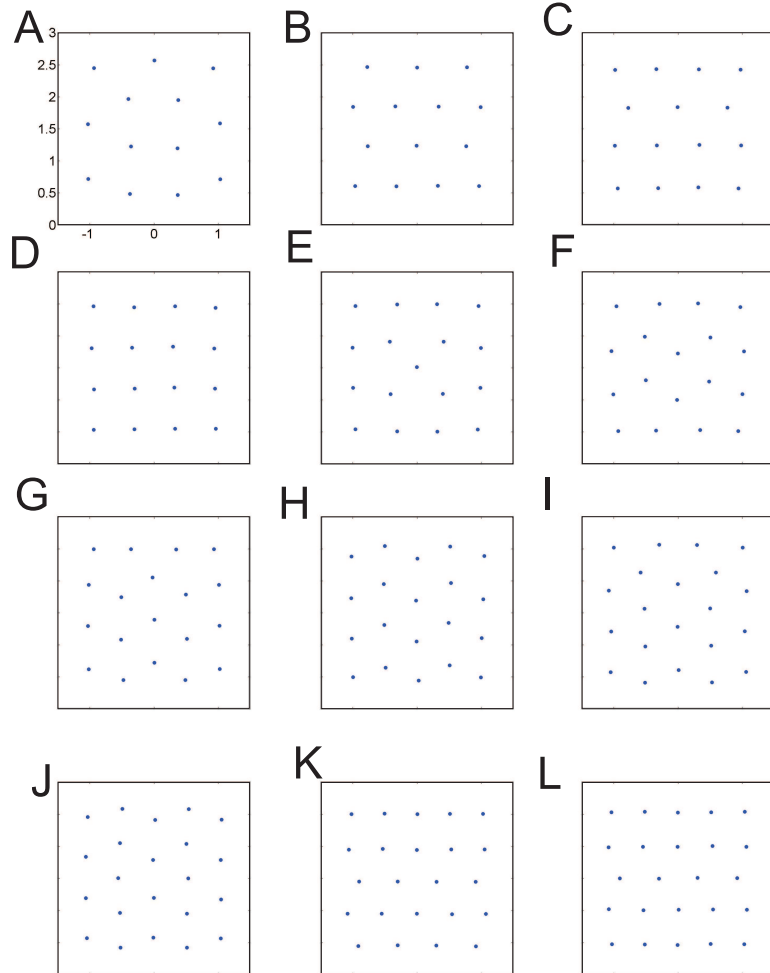


Figure 2.9: $A \sim L$ show the vortex configurations for vorticity L varied from 13 to 24, respectively. For $L = 16$, perfect square lattice is formed. For $L = 14, 20$ and 22 , perfect triangular lattice is formed. The states that $L = 15, 23$ or 24 , both triangular and square lattices are found. Since the penetrated field decays fast as the position varies from the boundary to the center, the triangular lattice caused by the vortex-vortex interaction is formed near the center while the square lattice is formed near the boundary (e.g., C,E-L). All the states are trying to share the symmetry axis with the sample.

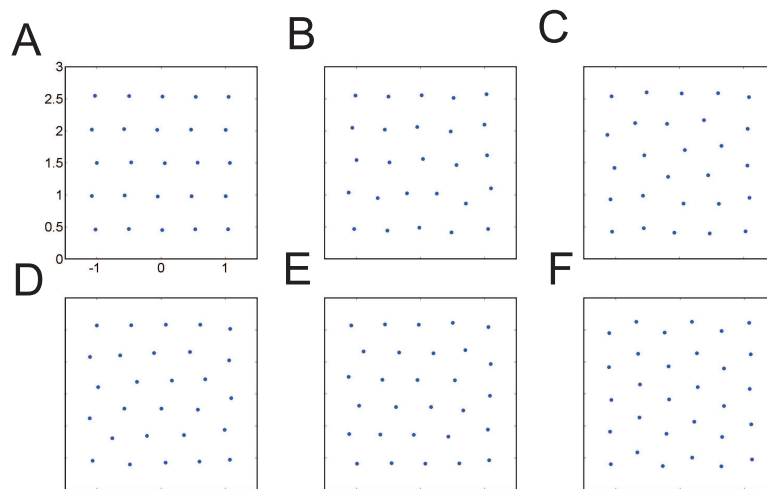


Figure 2.10: $A \sim F$ show the vortex configurations for vorticity L varied from 25 to 30, respectively. As the vorticity increases, the distance between the vortices decreases and the interaction increases fast which is more important than the effect of boundaries. The state with $L = 25$, the square lattice is not as perfect as the states with $L = 1, 4, 9, 16$. It is actually a little bit twisted and shows some tendency to form the triangular lattice. For large L , the patterns are mainly composed of triangular lattice distorted near the boundaries.

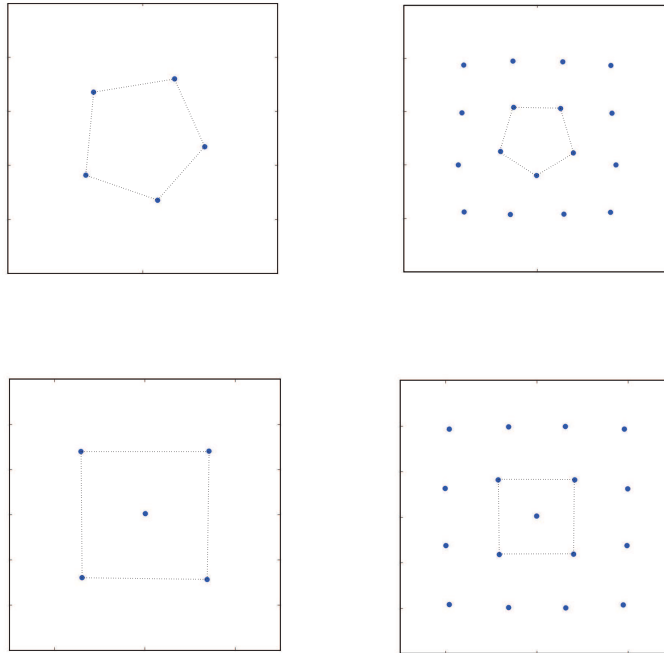


Figure 2.11: Possible states for the vorticity $L = 5, 17$, respectively. For $L = 17$, twelve vortices form a shell and the rest five vortices form a pentagon or a square with one vortex in the center.

Ground State Vs Metastable states

For a give vorticity, we can have many possible configurations. Let consider the case of $L = 5$. From our calculation, it follows that five vortices can form either a pentagon or a C_4 -symmetric pattern with one vortex in the center and the other four forming a square as shown in Fig. 2.11. In order to examine which one is more stable, we investigate the free energy as a function of the displacement of the vortex position. We change the position of one vortex of the pentagon along the line between the vortex and the center of the sample and other vortices' positions are determined by minimizing the free energy. This procedure gives the barrier between the two states. In Fig. 2.12, we show the change in the free energy associated with the re-arrangement of the pentagon-like configuration (denote it as (5)) to the configuration with one vortex in the center (1,4), as shown in Fig. 2.11 and the insets of Fig. 2.12. We move one of the vortices of configuration (5) towards the center, while other vortices adjust themselves accordingly, to minimize the energy. We see that the motion of vortex C is accompanied with the lowest energy barrier. This is because vortices A, B, D and E are already close to their final positions in state (1,4). Moving vortices B or D lead to a higher energy barrier. Finally, moving vortex A or E to the center associated with the highest barrier and passing via a saddle point (jump in $G - G_0$).

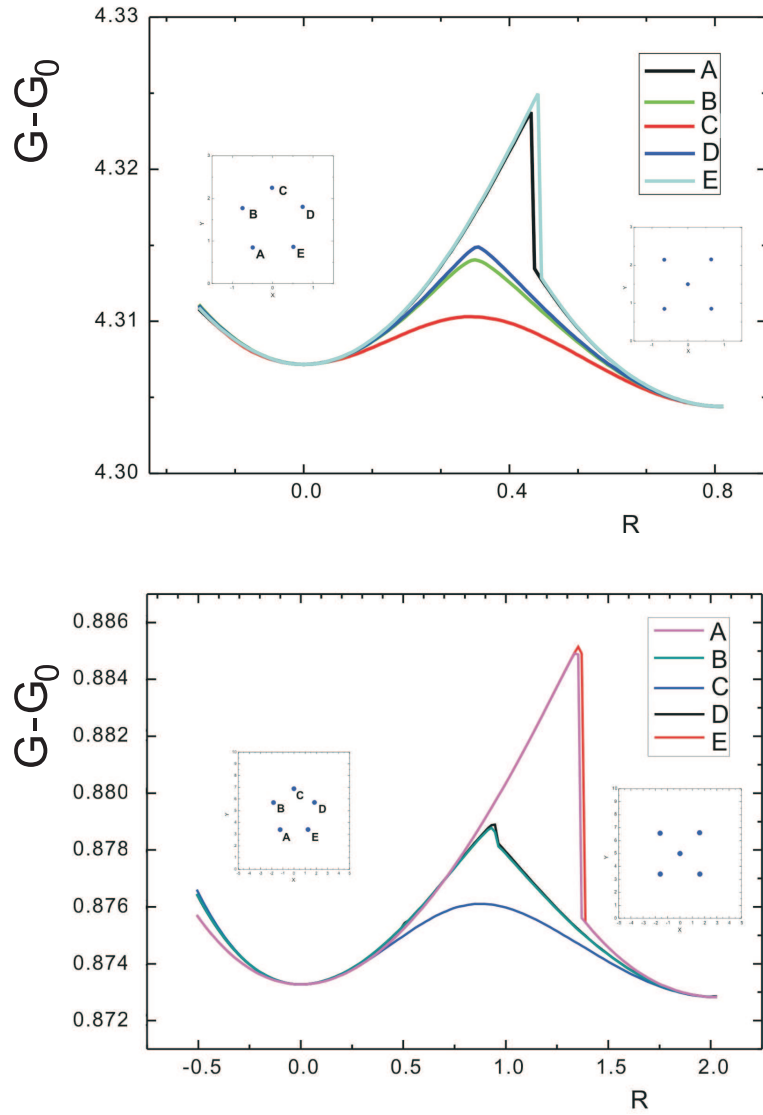


Figure 2.12: The change of the free energy ($G - G_0$) versus the displacement R of one of the vortex in the initial pentagon-shaped configuration from its initial position. G_0 is the free energy associated with external magnetic field and the vortex cores, which is independent of the vortices' position. The two stable states are shown in the insets and the vortices are labeled by A~E. The size of the two squares are $a = 3\lambda$ and $a = 10\lambda$. For both cases, the barrier exists, and the configuration with one vortex in the center has a lower energy than the pentagon-like pattern.

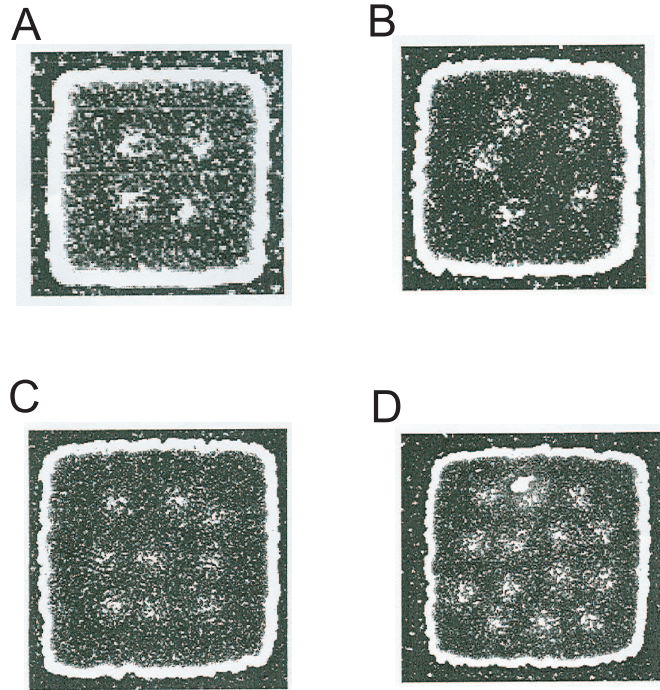


Figure 2.13: The experimental images of vortex configurations in mesoscopic Nb squares. From A to D, the vorticity $L = 4, 5, 9, 14$, respectively. For $L = 4, 9$, they almost form perfect square lattices the same as we obtained in our simulation. For $L = 5$, we also observed the same states (see Fig. 2.11), which is considered as a metastable state. For $L = 14$, in our calculation, we also have a certain chance to obtain this state (more frequent for the squares with the side $a = 10\lambda$) (After Ref. [60].)

2.2.3 Comparison with experiment

In Fig. 2.13, we show the experimental images in mesoscopic Nb squares done by Grigorieva *et al.* [60] obtained using the Bitter decoration technique. The vortex patterns obtained in our simulation agree with those patterns of the vortex states in mesoscopic Nb squares. We see that in Fig. 2.13, the states for $L = 4, 9$ form the square lattices, while for $L = 5$, a pentagon is formed. The state for $L = 14$ is also obtained in our simulation. But the state shown in Fig. 2.9 (B) is obtained more frequently, especially for mesoscopic squares.

Chapter 3

Vortex states in equilateral triangles

3.1 Theoretical formalism

3.1.1 Solution of the London equation for an equilateral triangle

For an equilateral triangle, we use the same approximate boundary condition as we did in square. And we notice that the result we obtained in Eq. (2.28) is general, i.e., applicable to any geometry of the sample. In the case of a triangle, the integral in Eq. (2.28) should be taken over the hole triangle, that is

$$h(x', y') = H \left[1 - \int_0^{\sqrt{3}a/2} dy \int_{a/2-y/\sqrt{3}}^{a/2+y/\sqrt{3}} dx G(x, y, x', y') \right] + \Phi_0 \sum_i G(x_i, y_i, x', y'), \quad (3.1)$$

where we have considered the problem in Cartesian coordinates (see Fig. 3.1), and a is the length of the side. The triangular coordinates (u, v, w) were defined as follows:

$$\begin{aligned} u &= r - y, \\ v &= \frac{\sqrt{3}}{2} \cdot \left(x - \frac{a}{2}\right) + \frac{1}{2} \cdot (y - r) \\ w &= -\frac{\sqrt{3}}{2} \cdot \left(x - \frac{a}{2}\right) + \frac{1}{2} \cdot (y - r) \end{aligned} \quad (3.2)$$

in Ref. [59]. Here, $r = \frac{a}{2\sqrt{3}}$ is the inradius of the triangle. The corresponding Green's function G associated with London equation satisfies the equation

$$-\lambda^2 \nabla^2 G + G = \delta(x - x') \delta(y - y'), \quad (3.3)$$

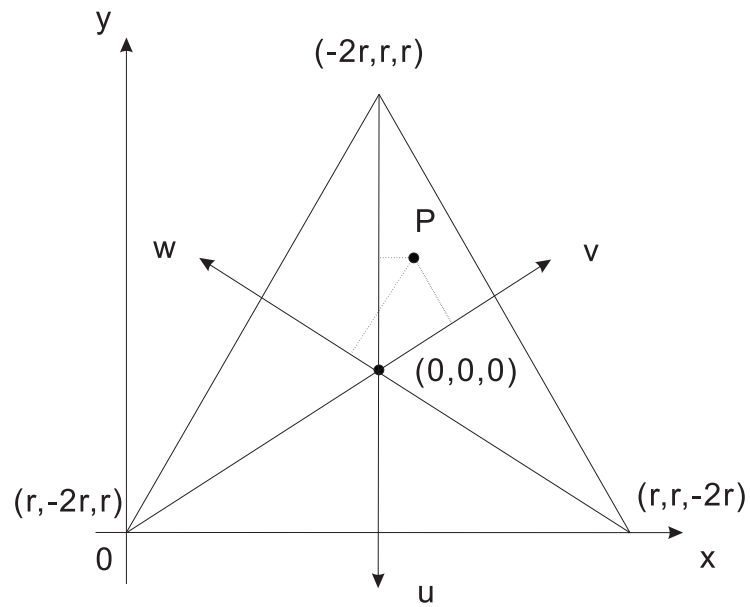


Figure 3.1: The coordinate system of the triangle. $r = \frac{a}{2\sqrt{3}}$ is the inradius of the triangle. The three boundaries in triangular coordinate system are simply given by $u = r$, $w = r$ and $v = r$, respectively. The external magnetic field is along the z -axis which is perpendicular to this surface, and its value is assumed to be constant outside the sample region.

and the boundary condition

$$G(r, v, w) = G(u, r, w) = G(w, v, r) = 0. \quad (3.4)$$

To satisfy this condition, we expand G in the series

$$G(x, y; x', y') = \sum_{m=1}^{\infty} \left\{ A_m \phi_s^{m,m}(x, y) \phi_s^{m,m}(x', y') \right. \\ \left. + \sum_{n=m+1}^{\infty} [B_{m,n} \phi_s^{m,n}(x, y) \phi_s^{m,n}(x', y') + C_{m,n} \phi_a^{m,n}(x, y) \phi_a^{m,n}(x', y')] \right\} \quad (3.5)$$

since $\phi_s^{m,n}(x, y)$ and $\phi_a^{m,n}(x, y)$ given in Ref. [59] are orthonormal and complete. The δ -function in Eq. (3.3) can also be expanded, that is

$$\delta(x - x') \delta(y - y') = \sum_{m=1}^{\infty} \left\{ \phi_s^{m,m}(x, y) \phi_s^{m,m}(x', y') \right. \\ \left. + \sum_{n=m+1}^{\infty} [\phi_s^{m,n}(x, y) \phi_s^{m,n}(x', y') + \phi_a^{m,n}(x, y) \phi_a^{m,n}(x', y')] \right\}. \quad (3.6)$$

The coefficients in Eq. (3.5) can be determined using Eq. (3.3),

$$A_m = \frac{1}{-\lambda^2 \epsilon_{m,m} + 1}; \quad B_{m,n} = C_{m,n} = \frac{1}{-\lambda^2 \epsilon_{m,n} + 1}. \quad (3.7)$$

Here $\epsilon_{m,n} = \frac{4}{27} \left(\frac{\pi}{r}\right)^2 [m^2 + mn + n^2]$ is the eigenvalue of the Laplace operator. We thus obtain the Green's function. The integral of the Green's function in Eq. (3.1) gives the magnetic field distribution in the Meissner case. When $m \neq n$,

$$\int \int d\tau \phi_s^{m,n}(x, y) = \int \int d\tau \phi_a^{m,n}(x, y) = 0, \quad (3.8)$$

and we also notice that it is more convenient to use the not normalized functions in Ref. [59]. Thus, the magnetic field is given by

$$h(x', y') = H \left[1 - \sum_{m=1}^{\infty} \frac{2}{\pi m} \cdot \frac{1}{-\lambda^2 \epsilon_{m,m} + 1} T_s^{m,m}(x', y') \right] \\ + \Phi_0 \sum_i G(x_i, y_i, x', y'). \quad (3.9)$$

The first part is the contribution of the penetrated external field and the second part is a sum of contribution of all vortices and their images. The first term contains only the eigenfunctions with $m = n$ which have the C_3 symmetry. The second term include the Green's function is tedious, because we have to take the summation over two indices. We do not intend to proceed as we did in the case of rectangle. Instead, we will use the images method, which is much more favorable. For the equilateral triangle, the distribution of the images is quite similar to that in a square (see Fig. 3.2), although more images should be considered here.

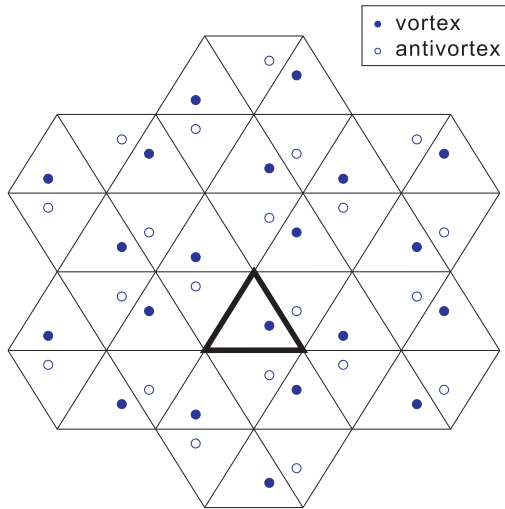


Figure 3.2: Vortex images in an equilateral triangle. The density of images we used for the triangular boundary (thick black lines) is larger than that in a square, more images should be considered here as compared to the case of a square.

3.2 Numerical results

3.2.1 Meissner state in triangular samples

For the equilateral triangle, the first term in Eq. (3.9) gives the magnetic field distribution in the Meissner case (see Fig. 3.3). This field distribution is also minimum at the center which is the same as in a square or disk sample.

3.2.2 Vortex patterns in triangular samples

For triangular samples, we proceed in the same way as we did for the square by using the image method. The vortex patterns are shown in Fig. 3.4 and 3.5. For $L = 1, 3, 6, 10, 15, 21$, perfect triangular lattice which has the C_3 symmetry is formed as we expected. For $L = 4$, three vortices form a triangle and one is located at the center, which also has the triangle's symmetry. For the other cases except $L = 5, 20$, the configurations always try to adapt to one of the three symmetry axes of the triangle. As we increase the vorticity, the vortices tend to fill the region near the edge first, since it is much wider than that near the center. The patterns clearly show the competition between the vortex-vortex interaction which tries to form triangular lattice and the effect of the surface, which tries to add its own symmetry to the configuration.

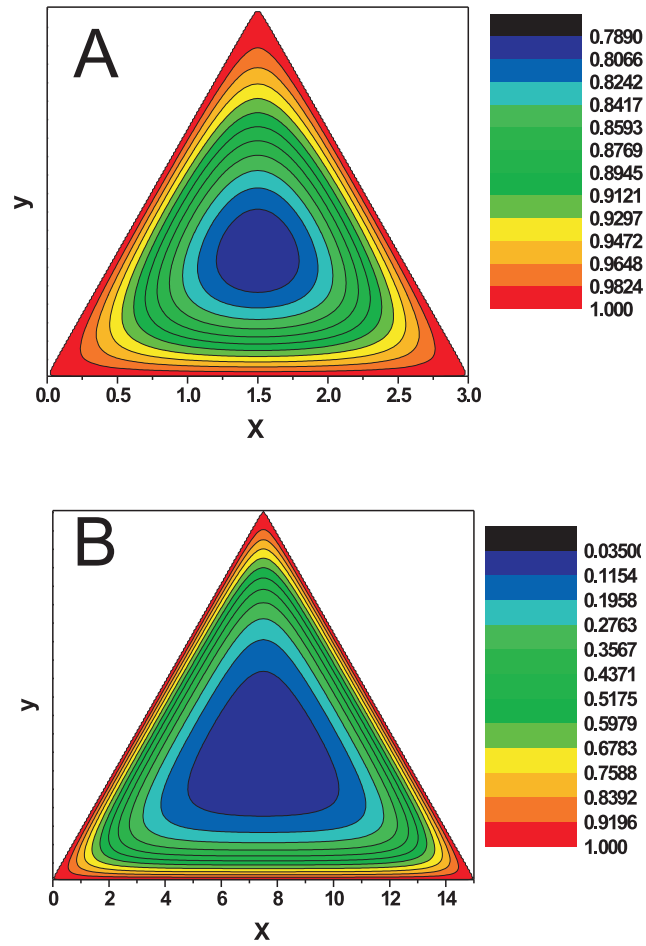


Figure 3.3: The magnetic field distribution in the Meissner state in equilateral triangles with the length of the side $a = 3$ (A) and $a = 15$ (B), respectively. For mesoscopic sample, the field is penetrated everywhere, while for microscopic sample, it dropped almost to zero near the center.

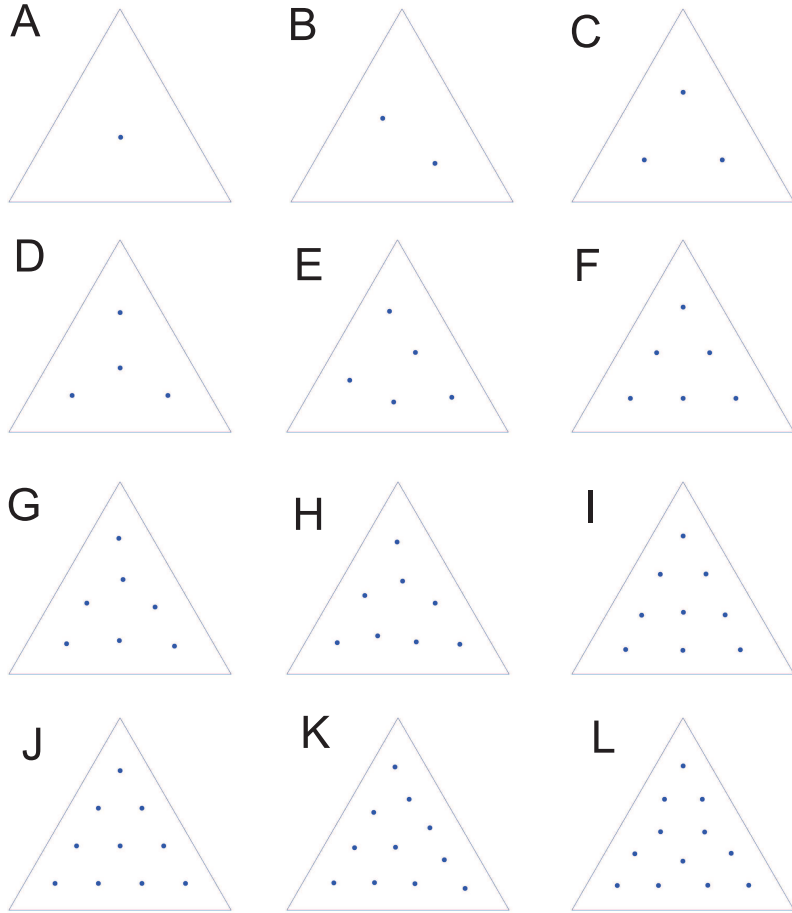


Figure 3.4: $A \sim L$ show the vortex configurations for the vorticity L varied from 1 to 12, respectively. The patterns show that, except $L = 5$, other states share at least one symmetry axis with the sample. The layers along the symmetry axis increase as L increase. For $L = 1, 3, 6, 10$, the triangular lattice is formed as we expect. Other states are also trying to form triangular lattice although the number of vortices is incompatible with the C_3 -symmetry. As the vorticity increases, the vortices try to fill the region near the boundary first, since it is wider than near the center.

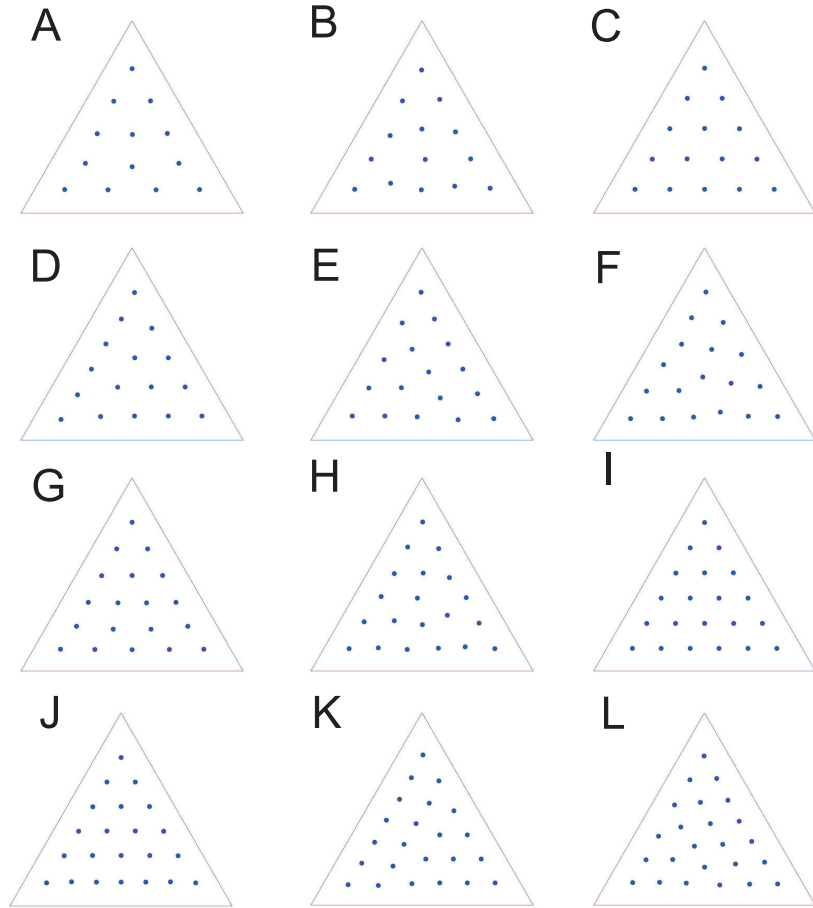


Figure 3.5: $A \sim L$ show the vortex configurations for the vorticity L varied from 13 to 24, respectively. The stats with $L = 15, 21$, which are compatible with the C_3 -symmetry, are formed by perfect triangular lattice. From $L=15$ to 21, the number of vortices near the boundary always increases first and the region near the center is filled last.

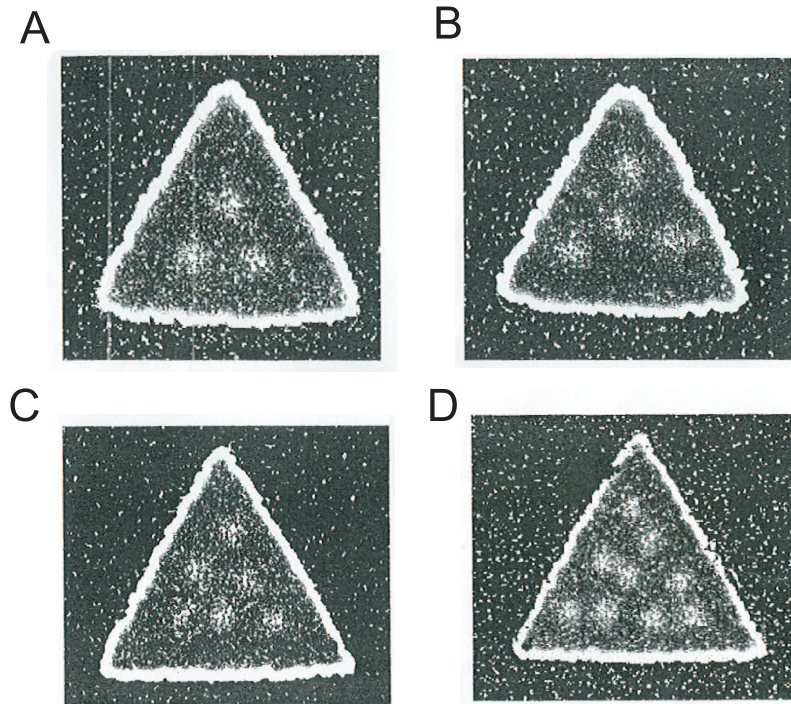


Figure 3.6: The experimental images of vortex configurations in mesoscopic Nb triangles. A to D show the vortex states with $L = 3, 4, 6, 9$, respectively, which agree with the states C, D, F, I in Fig. 3.4 (After Ref. [60]).

3.2.3 Comparison with experiment

In Fig. 3.6, we see that the experimental images of vortex states in mesoscopic Nb triangles found by Grigorieva *et al.* [60] also agree with our simulation shown in Fig. 3.4.

Chapter 4

Conclusions

In this Thesis, I investigated the vortex configurations in mesoscopic superconducting squares and equilateral triangles within the London theory, using the Green's function method for solving the London equation and the image method for calculating the free energy distributions, and the Molecular-Dynamics simulations to obtain vortex patterns in the square and triangular samples.

The main goals of this study included education, methodology and research. During my work on the Thesis, I learned the theory of superconductivity in mesoscopic systems — the nucleation of superconducting phase, penetration of vortices in mesoscopic samples induced by an external applied field, generation of antivortices, symmetry-induced vortex-antivortex states, the dynamics of vortices in superconductors with artificial pinning arrays, etc., — from literature, including many works of my promotors and the knowledge and experience accumulated in the Condensed Matter Theory (CMT) group in the theory of superconductivity in mesoscopic systems. I learned theoretical methods to study vortex matter in superconductors including the Ginzburg-Landau and London theories, the Greens' function method for solving the London equations, the image technique applied to vortices in finite-size samples, the Molecular-Dynamics simulations for studying the vortex dynamics in superconductors. In particular, I studied the application of these methods for the investigation of vortex matter in mesoscopic superconductors where the effects of boundaries play a crucial role making these systems quite different from bulk superconductors.

Vortex patterns in mesoscopic superconductors of various geometries were extensively studied theoretically during last few decades. Many works were devoted to the investigation of various vortex states in mesoscopic disks, which, in spite their simple shape, provide a rich variety of vortex states and effects including multivortex states and giant vortex states, transitions between them, formation of vortex shells, and also the phenomena induced by confinement combined with the effect of pinning such as pinning-induced clustering and formation of giant vortices, etc. Furthermore, a mesoscopic superconducting disk is a unique sample to study the dynamics of vortex matter under the action of a gradient Lorentz force induced by an external current (in Corbino

setup). This allows one to study elastic moduli and the onset of plasticity in vortex lattice.

The interest to samples with geometry other than disks was induced by the possibility to study the interplay between the circular symmetry (C_∞) of the magnetic field and a discrete symmetry of noncircular-shaped polygons (e.g., squares (C_4), triangles (C_3), etc.). In this case, the formation of vortex patterns is governed by the intervortex interaction, which results in the triangular Abrikosov vortex lattice in bulk superconductors, and by the interaction of vortices with symmetric boundaries of the sample which tend to impose their symmetry on the vortex configurations. As a result of this interplay, symmetric vortex configurations and even novel symmetry-induced vortex states with antivortices can be generated in mesoscopic superconductors of noncircular geometry.

While a considerable progress has been achieved in the understanding of the vortex matter in mesoscopic systems, and a large number of theoretical studies were published in the field, there exist only a limited number of experimental studies on *direct* visualization of calculated vortex states (in many experiments integral (e.g., the magnetization, the superconducting-to-normal phase boundary) or dynamical (e.g., transport current, $I - V$ -curves, critical current) characteristics are usually measured which provide *indirect* information on the vortex states in the sample and very often can be treated in different ways). The main experimental restriction is the resolution (i.e., the spatial resolution and the contrast) of the existing methods of vortex visualization, which is still in many cases insufficient to resolve separate vortices on the scales of the order of few (tens) nanometers.

Recently, experiments on the *direct vortex visualization* using the Bitter decoration technique were performed by I.V. Grigorieva and co-workers at the University of Manchester (UK). They for the first time observed vortex shell structures in mesoscopic Nb disks (in clean disks with weak underlying pinning) [40] and also the pinning-induced clustering and giant-vortex formation in disks with strong disorder [9] (this work was done in collaboration with the CMT group). The new experiments on vortex shells visualization, on the one hand, verified early theoretical predictions and, on the other hand, they raised new questions since some of the observed configurations did not match those early predicted in theory. This in its turn induced new theoretical investigations. Thus it was shown in Ref. [8] that the discrepancy between some experimentally observed vortex configurations and the previous theoretical studies can be explained by a size dependence of vortex configurations: in rather large disks the effects of the London screening lead to the change of the confinement energy (as compared to small mesoscopic disks) and a re-distribution of vortices.

Although not described in detail in Ref. [40], the experiments were performed with large arrays of disks and also of samples of other shape, squares and triangles. Some of preliminary results of the Manchester group on vortex configurations observed in squares and triangles were reported (e.g., [60]), and these experiments are in progress [61].

Here we theoretically analyze vortex configurations in mesoscopic supercon-

ducting squares and equilateral triangles. We treat vortices within the London theory, and we solve the London equation analytically using the Green's function method. Note that our derivation of the London free energy functional at the initial steps is similar to the formalism developed earlier in Ref. [55]. However, we do not use approximations as the authors of Ref. [55]: they considered an elongated rectangle which allowed them to simplify the problem. Our result is more general and applicable to rectangles with any aspect ratio between the sides a and b . We also apply the image technique as an alternative way to calculate the distribution of the free energy in the samples. As a result of the solution of the London equation, we obtain the field of forces which act on a vortex at any position in the sample. The total force includes the contributions from the vortex-vortex and vortex-surface interactions, and the self-interaction with its own image.

An important feature of the obtained solutions is that in principle they are applicable to samples of any size, which allows us to describe vortex patterns in *different regimes* (e.g., the crossover from “thin mesoscopic” to “thick macroscopic” regimes [8]) within *one* model. In other words, the model is applicable to both small mesoscopic samples, where one can neglect the screening effects, as well as to large samples where the London screening effects are important and lead to a re-arrangement of vortex configurations.

The obtained distributions of the total force acting on a vortex are used to compute stable vortex configurations in square- and equilateral-triangle-shaped samples. The results of our calculations for squares and equilateral triangles are summarized in Table. 4.1. For comparison, we also present in Table. 4.1 the results of shell filling in disks obtained experimentally [40] and theoretically [8]. Note that in samples of noncircular geometry we do not have well-defined shells as in disks. Instead, the obtained configurations often look like fragments of a vortex lattice (square or triangular) distorted by the sample boundaries. Although in order to classify them, we still use the denotations used for the description of shells in disks.

According to our calculations, for some vorticities L the obtained vortex configurations can have different modifications. To distinguish between the ground-state and metastable configurations, we analyze the free energy associated with different configurations and its change during a continuous transition from one configuration to another. For example, we show that in a square for $L = 5$ there are two vortex configurations: (i) a pentagon-shaped configuration (5), and (ii) a symmetric “two-shell” configuration (1,4) with one vortex at the center and four near the corners of the square. The free energy analysis shows that (1,4) is the ground-state configuration. Similarly, for vorticity $L = 17$, vortices in a square can arrange themselves either in a “two-shell” configuration (5,12), or in a “three-shell” configuration (1,4,12). We compared the obtained vortex patterns with available experimental data and found that they are in a good agreement.

L	Disks [8, 40]	Squares	Triangles
1	(1)	(1)	(1)
2	(2)	(2)	(2)
3	(3)	(3)	(3)
4	(4)	(4)	(1,3)
5	(5)	(5), (1,4)	(5)
6	(1,5)	(1,5) ^d	(6) [(3,3)]
7	(1,6)	(1,6)	(4,3) ^d
8	(1,7)	(1,7)	(5,3) ^d
9	(2,7)	(1,8)	(1,5,3)
10	(2,8)	(2,8)	(1,6,3) [(1,9)]
11	(3,8)	(3,8)	(1,7,3)
12	(3,9)	(2,10)	(3,6,3)
13	(4,9)	(4,9)	(2,8,3)
14	(4,10)	(3,11)	(2,9,3)
15	(4,11)	(3,12)	(3,9,3) [(3,12)]
16	(5,11)	(4,12)	(3,10,3)
17	(1,5,11)	(5,12), (1,4,12)	(17) ^d
18	(1,5,12)	(4,14)	(18) ^d
19	(1,6,12)	(1,4,14)	(19) ^d
20	(1,7,12)	(1,5,14) ^d	(20) ^d
21	(1,7,13)	(1,5,15) ^d	(3,9,6,3)
22	(1,8,13)	(4,4,14) ^d	(22) ^d
23	(2,8,13)	(1,6,16)	(23) ^d
24	(1,5,11)	(1,7,16)	
25	(3,8,14)	(1,8,16)	
26	(3,9,14)	(1,8,17)	
27	(3,9,15)	(2,8,17) ^d	
28	(3,10,15)	(2,9,17) ^d	
29	(4,10,15)	(3,8,18) ^d	
30	(4,10,16)	(3,8,19) ^d	

Table 4.1: Filling of the “shells” in vortex configurations for different L in squares and triangles. In first column, for comparison the filling of the shells is shown for disks. Note that in squares and triangles the “shells” are not as well defined as in disks. In some cases square- or triangular-shaped “shells” can be easily distinguished, but in some cases the distributions look rather as a distorted vortex lattice (we denote such unclear cases with ^d). In triangles for $L > 2$ there are always vortices in the corners which can be interpreted as an “outer shell”; alternatively, they can be counted together with “inner” vortices as one single “shell”, therefore, we give two possible configurations in [square brackets]. When two different configurations are possible for the same vorticity L , we show both of them, and the first one is the ground-state energy configuration, and the second one is a metastable configuration.

Bibliography

- [1] P.G. de Gennes, *Superconductivity of metals and Alloys*, Addison-Wesley Publishing company, Reading, Massachusetts, 1989.
- [2] M. Tinkham, *Introduction to superconductivity*, Second Edition, McGraw-Hill, New York, 1996.
- [3] V.V. Moshchalkov, L. Gielen, C. Strunk, R. Jonckheere, X. Qiu, C. van Haesendonck, and Y. Bruynseraede, *Nature (London)* **373**, 319 (1995).
- [4] V.M. Fomin, V.R. Misko, J.T. Devreese, and V.V. Moshchalkov, *Solid State commun.* **101**, 303 (1997); *Phys. Rev. B* **58**, 11703 (1998).
- [5] P.S. Deo, V.A. Schweigert, F.M. Peeters, and A.K. Geim, *Phys. Rev. Lett.* **79**, 4653 (1997).
- [6] V.A. Schweigert and F.M. Peeters, *Phys. Rev. Lett.* **83**, 2409 (1999).
- [7] V.A. Schweigert and F.M. Peeters, *Phys. Rev. Lett.* **81**, 2783 (1998).
- [8] V.R. Misko, B. Xu, and F.M. Peeters, *Phys. Rev. B* **76**, 024516 (2007).
- [9] W. Escoffier, I.V. Grigorieva, V.R. Misko, B.J. Baelus, F.M. Peeters, S.V. Dubonos, and L.Ya. Vinnikov, *Phys. Rev. Lett.* **99** (2007), in press.
- [10] L. F. Chibotaru, A. Ceulemans, V. Bruyndoncx, and V.V. Moshchalkov, *Nature (London)* **408**, 833 (2000); *Phys. Rev. Lett.* **86**, 1323 (2001).
- [11] V.R. Misko, V.M. Fomin, J.T. Devreese, and V.V. Moshchalkov, *Physica (Amsterdam)* **369C**, 361 (2002).
- [12] B.J. Baelus, F.M. Peeters, and V.A. Schweigert, *Phys. Rev. B* **65**, 104515 (2002).
- [13] V.R. Misko, V.M. Fomin, J.T. Devreese, and V.V. Moshchalkov, *Phys. Rev. Lett.* **90**, 147003 (2003).
- [14] M. Poza, E. Bascones, J. G. Rodrigo, N. Agraït, S. Vieira, and F. Guinea, *Phys. Rev. B* **58**, 11173 (1998).

- [15] V.R. Misko, V.M. Fomin, and J.T. Devreese, Phys. Rev. B **64**, 014517 (2001).
- [16] R. Geurts, M.V. Milošević, and F.M. Peeters, Phys. Rev. Lett. **97**, 137002 (2006).
- [17] M.V. Milošević and F.M. Peeters, Phys. Rev. Lett **93**, 267006 (2004); **94**, 227001 (2005).
- [18] R.Wördenweber, P.Dymashevski, V.R. Misko, Phys. Rev. B **69**, 184504 (2004).
- [19] J. Eisenmenger, Z.-P. Li, W.A.A. Macedo, I.K. Schuller, Phys. Rev. Lett. **94**, 057203 (2005).
- [20] M. Baert, V.V. Metlushko, R. Jonckheere, V.V. Moshchalkov, and Y. Bruynseraede, Phys. Rev. Lett., **74**, 3269 (1995); V.V. Moshchalkov, M. Baert, V.V. Metlushko, E. Rosseel, M.J. Van Bael, K. Temst, R. Jonckheere, and Y. Bruynseraede, Phys. Rev. B **54**, 7385 (1996); K. Harada, O. Kamimura, H. Kasai, T. Matsuda, A. Tonomura, and V.V. Moshchalkov, Science **274**, 1167 (1996).
- [21] A. Bezryadin and B.Pannetier, J. Low Temp. Phys. **102**, 73 (1996); A. Bezryadin, Yu. N. Ovchinnikov, and B. Pannetier, Phys. Rev. B **53**, 8553 (1996).
- [22] J. E. Villegas, Sergey Savel'ev, Franco Nori, E. M. Gonzalez, J. V. Anguita, R. García, and J. L. Vicent , Science **302**, 1188 (2003); M.I. Montero, Johan J. Åkerman, A. Varilci, and Ivan K. Schuller, Europhys. Lett. **63**, 118 (2003).
- [23] V. Misko, S. Savel'ev, F. Nori, Phys. Rev. Lett. **95**, 177007 (2005); V.R. Misko, S. Savel'ev, F. Nori, Phys. Rev. B **74** 24522 (2006).
- [24] M. Kemmler, C. Gürlich, A. Sterck, H. Pöhler, M. Neuhaus, M. Siegel, R. Kleiner, and D. Koelle, Phys. Rev. Lett. **97**, 147003 (2006).
- [25] A.V. Silhanek, W. Gillijns, V.V. Moshchalkov, B.Y. Zhu, J. Moonens, and L.H.A. Leunissen, Appl. Phys. Lett. **89**, 152507 (2006).
- [26] L.R.E. Cabral, B.J. Baelus, and F.M. Peeters, Phys. Rev. B **70**, 144523 (2004).
- [27] M.V. Milošević and F.M. Peeters, Phys. Rev. B **68**, 024509 (2003).
- [28] V.A. Schweigert and F.M. Peeters, Phys. Rev. B **57**, 13817 (1998).
- [29] V.A. Schweigert and F.M. Peeters, Phys. Rev. B **60**, 3084 (1999).
- [30] B.J. Baelus, F.M. Peeters, and V.A. Schweigert, Phys. Rev. B **63**, 144517 (2001).

- [31] A.K. Geim, I.V. Grigorieva, S.V. Dubonos, J.G.S. Lok, J.C. Maan, A.E. Filippov, and F.M. Peeters, *Nature (London)* **390**, 256 (1997).
- [32] Yu.E. Lozovik and E.A. Rakoch, *Phys.Rev. B* **57**, 1214 (1998).
- [33] A.A. Abrikosov, *Fundamentals of the Theory of Metals* (North-Holland, Amsterdam, 1986).
- [34] A.I. Buzdin and J.P. Brison, *Phys. Lett. A* **196**, 267 (1994)
- [35] J.J. Palacios, *Phys. Rev. B* **58**, R5948 (1998).
- [36] A.K. Geim, S.V. Dubonos, J.J. Palacios, I.V. Grigorieva, M. Henini, and J.J. Schermer, *Phys. Rev. Lett.* **85**, 1528 (2000).
- [37] A. Kanda,¹ B. J. Baelus, F. M. Peeters, K. Kadowaki, and Y. Ootuka¹, *Phys. Rev. Lett.* **93**, 257002 (2004).
- [38] M.V. Milošević, S.V. Yampolskii, and F.M. Peeters, *Phys. Rev. B* **66**, 024515 (2002).
- [39] B.J. Baelus, L.R.E. Cabral, and F.M. Peeters, *Phys. Rev. B* **69**, 064506 (2004).
- [40] I.V. Grigorieva, W. Escoffier, J. Richardson, L.Y. Vin-nikov, S. Dubonos, and V. Oboznov, *Phys. Rev. Lett.* **96**, 077005 (2006).
- [41] B.J. Baelus, *Vortex Matter in Mesoscopic Superconductors*, Ph.D thesis (2002).
- [42] L.J. Campbell and R.M. Ziff, *Phys. Rev. B* **20**, 1886 (1979).
- [43] G.B. Hess, *Phys. Rev.* **161**, 189 (1967).
- [44] D. Stauffer and A.L. Fetter, *Phys. Rev.* **168**, 156 (1968).
- [45] H. Totsuji and J.L. Barrat, *Phys. Rev. Lett.* **60**, 2484 (1988).
- [46] V.M. Bedanov and F.M. Peeters, *Phys. Rev. B* **49**, 2667 (1994).
- [47] Y.-J. Lai and L. I, *Phys. Rev. E* **60**, 4743 (1999).
- [48] I.V. Schweigert, V.A. Schweigert, and F.M. Peeters, *Phys. Rev. Lett.* **84**, 4381 (2000); K. Mangold, J. Birk, P. Leiderer, and C. Bechinger, *Phys. Chem. Chem. Phys.* **6**, 1623 (2004).
- [49] V. Bruyndoncx, J.G. Rodrigo, T. Puig, L. Van Look, V.V. Moshchalkov, and R. Jonckheere, *Phys. Rev. B* **60**, 4285 (1999).
- [50] H.T. Jadallah, J. Rubinstein, and P. Sternberg, *Phys. Rev. Lett.* **82**, 2935 (1999).

- [51] Th. Schuster, H. Kuhn, E.H. Brandt, and S. Klaumüzer, Phys. Rev. B **56**, 3413 (1997); G.P. Mikitik and E.H. Brandt, *ibid.* **62**, 6800 (2000).
- [52] Bonča and V.V. Kabanov, Phys. Rev. B **65**, 012509 (2002).
- [53] A. S. Mel'nikov, I.M. Nefedov, D. A. Ryzhov, I. A. Shereshevskii, V.M. Vinokur, and P. P. Vysheslavtsev, Phys. Rev. B **65**, 140503 (2002).
- [54] T. Mertelj and V.V. Kabanov, Phys. Rev. B **67**, 134527 (2003).
- [55] E. Sardella, M. M. Doria, and P. R. S. Netto, Phys. Rev. B **60**, 13158 (1999).
- [56] A.L. Fetter, P. C. Hohenberg, and P. Pincus, Phys. Rev. **147**, 140 (1966).
- [57] Y. Mawatari and K. Yamafuji, Physica C **228**, 336 (1994).
- [58] J.B. Ketterson and S.N. Song, *Superconductivity* (Cambridge University Press, 1999).
- [59] Brian J. McCartin, SIAM Review **45**, 267 (2003).
- [60] I.V. Grigorieva, L.Ya. Vinnikov, S.V. Dubonos, V.A. Oboznov, A. Geim, *Direct observation of multiple metastable vortex states in mesoscopic Nb samples*, Talk at the 10th International Vortex Workshop (IVW-10), Tata Institute of Fundamental Research, Mumbai, India, January 9-14, 2005. Abstract Book, page T-2.
- [61] I.V. Grigorieva, Private communication.